CVC Tech.Rep. #78 July, 2004

Generalized Active Shape Models Applied to Cardiac Function Analysis

Jaume Garcia i Barnés

Computer Vision Center / Dept. Informatica (UAB)
Edifici O - Campus UAB
08193 Bellaterra (Barcelona)
jaumegb@cvc.uab.es

Advisor: **Petia Radeva**

Submitted to the Computer Vision Center
on July, 2004

Contents

Generalized Active Shape Models Applied to Cardiac Function Analysis

by

Jaume Garcia i Barnés

Abstract

Medical imaging is very useful in the assessment and treatment of many diseases. To deal with the great amount of data provided by imaging scanners and extract quantitative information that physicians can interpret, many analysis algorithms have been developed. Any process of analysis always consists of a first step of segmenting some particular structure. In medical imaging, structures are not always well defined and suffer from noise artifacts thus, ordinary segmentation methods are not well suited. The ones that seem to give better results are those based on deformable models. Nevertheless, despite their capability of mixing image features together with smoothness constraints that may compensate for image irregularities, these are naturally local methods, i. e., each node of the active contour evolve taking into account information about its neighbors and some other weak constraints about flexibility and smoothness, but not about the global shape that they should find. Due to the fact that structures to be segmented are the same for all cases but with some inter and intra-patient variation, the incorporation of a priori knowledge about shape in the segmentation method will provide robustness to it. Active Shape Models is an algorithm based on the creation of a shape model called Point Distribution Model. It performs a segmentation using only shapes similar than those previously learned from a training set that capture most of the variation presented by the structure. This algorithm works by updating shape nodes along a normal segment which often can be too restrictive. For this reason we propose a generalization of this algorithm that we call Generalized Active Shape Models and fully integrates the a priori knowledge given by the Point Distribution Model with deformable models or any other appropriate segmentation method. Two different applications to cardiac imaging of this generalized method are developed and promising results are shown.

Keywords: Cardiac Analysis, Deformable Models, Active Contour Models, Active Shape Models, Tagged MRI, HARP, Contrast Echocardiography.

1 Objective of the present Work

The aim of this work is to provide a general segmentation framework that allows to incorporate a priori knowledge to any well suited segmentation method thus improving its result, and which can be used in many medical applications and, in particular, for cardiac imaging analysis. We also deepen into the origins that motivate this analysis which is heart structure and physiology, diseases by which can be affected and image modalities that allow their assessment. In this work, each section is motivated by the previous one thus, they are distributed following a precise order.

- In **section 2**, we depict the heart structure and its physiology. In addition, we introduce the novel ventricular band theory that could explain myocardium function which has not been completely understood yet.
- In **section 3**, we list different diseases that can affect heart function and the risky factors that may cause them.
- In **section 4**, we enumerate the different imaging techniques that have been developed to analyze not only heart function and structure, but also any organ or tissue in the body. We depict their characteristics and drawbacks and finally we introduce the medical imaging projects in which we have been working on.
- In **section 5**, we motivate the use of automatic analysis tools that allow to extract information from the great amount of data provided by scan devices exposed in the previous section and we overview some segmentation methods based on deformable models.
- In **section 6**, we introduce the concept of Point Distribution Model, that allow to create compact models that represent the mean shape and the variation modes of a target structure. We also introduce the Active Shape Model algorithm that allow segmentation including a priori knowledge about shape. We depict its limitations and propose a general framework for image segmentation that we call Generalized Active Shape Models (GASM).
- In **section 7**, we apply our framework GASM to segment the myocardial structure in Contrast Echocardiography imaging.
- In **section 8**, we present a novel imaging technique, SPAMM tagged MRI, that allow the visualization of the trajectories that myocardium points follow due to heart beat. We overview some techniques used to analyze them and we deepen into HARP method which, in addition, will be used in our GASM to segment myocardium structure. Finally we present a simple and direct application extracted from data returned by the method, namely the rotation of different sectors of the myocardium. This can be used to characterize heart pathologies.
- In **section 9**, we present results of GASM performance in both Contrast Ecocardiography and SPAMM tagged MRI.
- In **section 10**, we expose the conclusions extracted from the whole work.
- In **section 11**, we finally enumerate the tasks that we did not have enough time to perform, and possible improvements.

2 Heart Structure and Physiology

2.1 Introduction

The heart is a strong muscular organ of the circulatory system, that constantly pumps blood throughout the body to deliver oxygen to the cells and which is able to contract and relax rhythmically throughout

a person's lifetime. The heart is located in the chest between the lungs, behind the sternum and above the diaphragm. It is surrounded by the *pericardium*, a fluid filled sac that surrounds the heart and the proximal ends of the *aorta*, vena cava and the *pulmonary* artery. Heart size of an adult person is about that of a fist, and its weight is about 250-300 g.

The heart consists of four chambers, four valves and various vessels bringing blood to and carrying it away from the heart by veins and arteries. The upper chambers are called the *left* and *right atria*, and the lower chambers are called the *left* and *right ventricles* (LV, RV). A wall of muscle called the *septum* separates the *left* and *right atria* and the *left* and *right ventricles* (Figure 1.a). The *atria* act as reservoirs for venous blood, with a small pumping action to assist ventricular filling. In contrast, the ventricles are the major pumping chambers for delivering blood to the pulmonary (*right ventricle*) and systemic (*left ventricle*) circulations (Figure 1.b). The LV is the largest and strongest chamber in the heart and does the majority of the work. The LV chamber walls are only about a half- inch thick, but they have enough force to push blood through the *aortic valve* and to the whole body, [36]. Four valves ensure that blood flows only one way, from *atria* to *ventricle* (*tricuspid* and *mitral* valves), and then to the arterial circulations (*pulmonary* and *aortic* valves).

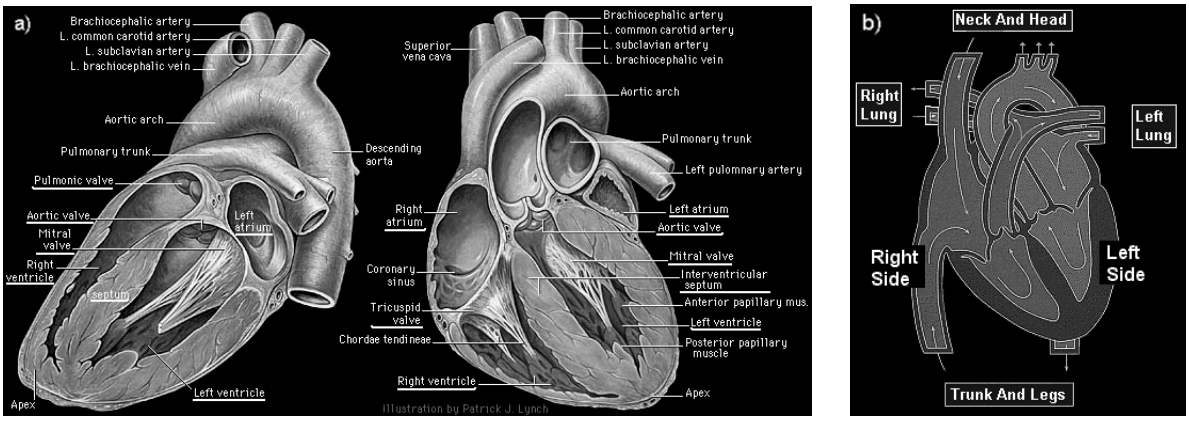

Figure 1: a) Gross anatomy of the heart. b) Heart physiology.

2.2 Ventricular Band Anatomy

Heart's cardiac cycle is composed of two basic functions, the contraction of the cardiac muscle (*myocardium*), *systole* and its relaxation, *diastole*. Nevertheless, how *myocardium* exactly works has not been completely well understood yet. Recent studies using advanced imaging techniques (such Spamm tagged MRI, which will discuss and analyze in further sections), have shown the complexity of its movement. Opposite extremes of the heart (top: *base*, bottom: *apex*), for instance, rotate in inverse directions, which was not obvious before these studies. This complex movement could be explained by the revolutionary theory of the ventricular band anatomy presented by Dr. Torrent-Guasp ([37], [38], [39], [40]). His dissection studies have lead to a description of the architecture of the LV and RV as the result of wrapping a unique muscular band that goes from the *pulmonary* artery to the *aorta*, applying to it a 180° torsion in its central part and joining the extremes (Figure 2.a).

Thus, LV and RV are the natural structures that appear as the consequence of this wrapping. This band is divided in four parts namely, *right ventricular segment* (RVS), *left ventricular segment* (LVS), *descendent segment* (DS) and *ascendent segment*(AS). The twirling of LVS and RVS, known as *basal bow*, delimits the external contour of the left and right cavities. The crossing of AS and DS, forms the *interventricular septum*. Figure 2.b depicts the distribution complexity of these segments.

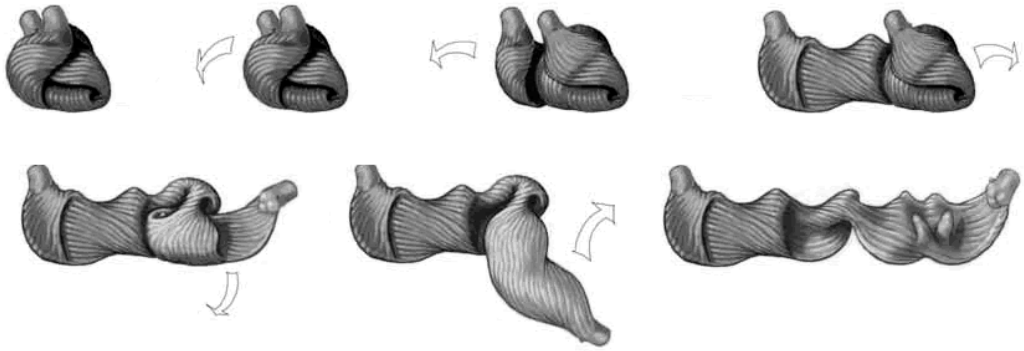

a)

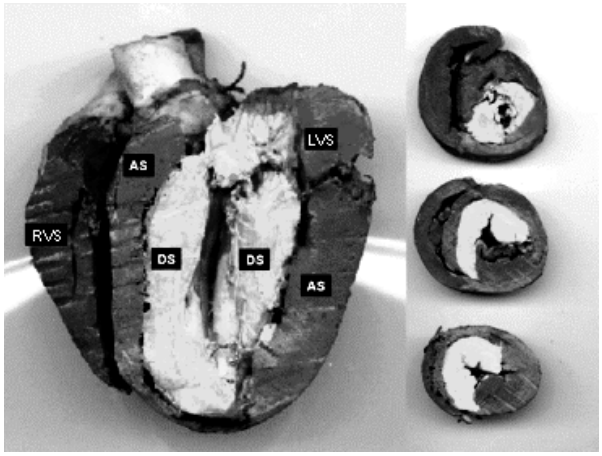

b)

Figure 2: a) Unwrapping process of the ventricular band. b) Spatial distribution of the different segments. Colored parts have been obtained by unwrapping a dissected heart, painting the segments and wrapping it again.

2.3 Ventricular Band Electromechanical Activation

It is known ([42], [41]) that electromechanical propagation along the *myocardium* is anisotropic and it mainly follows the same trajectories as the *myocardial fibers*. These, once the *ventricular band* is unwrapped, are appreciated to follow the band from one extreme to the other. This leads to the following *myocardial* activation sequence:

1^{st} **RVS:** Its activation pulse produces the *basal bow* to contract.

2^{nd} **LVS:** Its activation forms an external cylinder.

3^{rd} **DS:** Its activation stretches the basal bow in direction to the *appex* (the ending corner of the heart) thus reducing the ventricular capacity in the longitudinal direction. The consequence of this is the ventricular ejection.

4^{th} **AS:** Its activation generates a rapid ascendent displacement of the *base*. Recent observations have suggested that this may produce the necessary suction forces that fill the ventricles.

According to the existence of such *ventricular band*, it is thus reasonable to attribute *myocardial* complex movement to the electromechanical activation of the the different segments that compound the

band. However, how the contraction of a segment can turn to the elongation of the ventricles, still remains unknown.

This novel theory about the *ventricular band* is still not accepted by the whole physician community, thus many efforts are put in investigations that analyze *myocardial* function using the ultimate imaging technology (Spamm tagged MRI) so that this theory can be proven.

3 Cardiovascular Diseases: A Modern Epidemic

3.1 Introduction

Nowadays and since last century, industrialized countries have been experiencing huge social and economic transformations that have evoqued in radical changes in lifestyle. It is true that mortality has decayed notoriously, nevertheless the causes by which people die have also changed. Leaving aside traffic accidents and all types of cancer, cardiovascular diseases (CVD) have grown as the main death cause in Occident. Parallely, and not by chance, food habits is one of the factors that have changed most.

Before 1900, almost anyone died of heart diseases. Was in 1920 in the UUEE, when the country experienced its change from traditional lifestyle, that CVD started their incidency and currently, 80% of mortality is attributed to CVD. By the 1930's and 1940's, the death rate in the UUEE from atherosclerotic heart disease (AHD) was increasing at an alarming rate and it was reaching epidemical proportions. AHD is a process by which the arteries that supply blood to the heart (Figure 3.b) get narrowed and hardened due to fatty deposits made up of cholesterol. These deposits are called plaque. As shown in Figure 3.a, this slowly narrows the flow of blood through the vessel, and the muscle it supplies will not get enough blood and die.

The reasons for this epidemic were not completely clear. Some scientists were convinced that there was a single cause of atherosclerosis but most researchers favored the theory that there had to be due to multiple causes. After II World War, the first large-scale comprehensive study to determine the cause of AHD took place. It was called the Framingham Heart Study. It enrolled 5209 local residents ranging in age from 30 to 62 in study. Researchers began examining the participants every two years, and they continued to do so. In the early 1970's, 5135 adult offspring of the original participants joined the study. The Farmingham investigators established that there are, indeed, many factors (cardiovascular risk factors) that predispose an individual to the development of atherosclerosis.

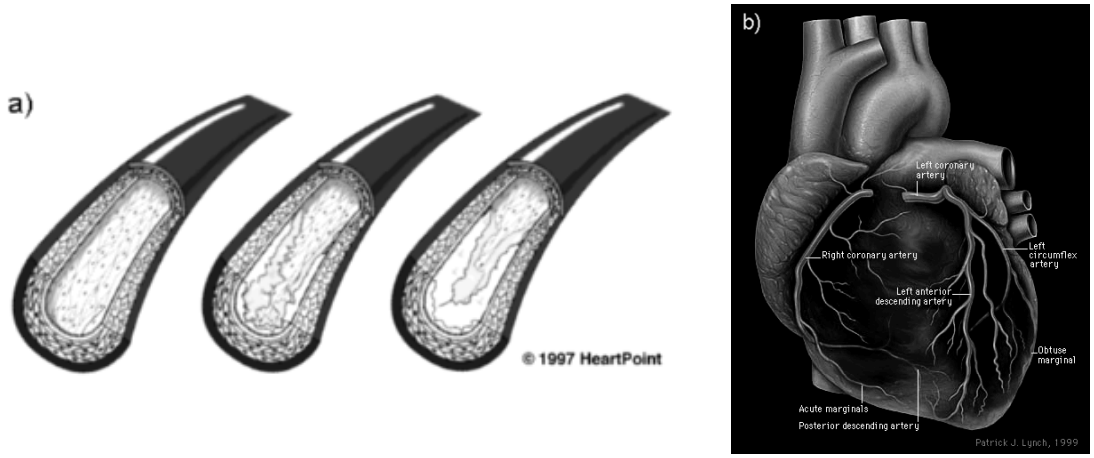

Figure 3: a) Process of occlusion suffered from an artery due to AHD. b) Main branches of the coronary tree that supply oxygen to the myocardium.

3.2 Cardiovascular Risk Factors

A cardiovascular risk factor (CVRF) is a condition that is associated with an increased risk of developing cardiovascular disease. The concept of CVRF has evolved since the Farmingham Heart Study, and new factors are periodically added to the list as our comprehension of the disease process grows and also as the society evolves. Regard that there are, for instance, new drugs as cocaine, that were not consumed before. CVRF can be divided in two groups: those that can be changed and those that cannot. As instances of the first group we have:

- **High Blood Pressure (*hypertension*)**: Blood pressure is the force in the arteries when the heart beats (*systolic* pressure) and when the heart is at rest (*diastolic* pressure). It is measured in millimeters of mercury (mm Hg). High blood pressure (or *hypertension*) is defined in an adult as a blood pressure greater than or equal to 140 mm Hg systolic pressure or greater than or equal to 90 mm Hg diastolic pressure.

  High blood pressure directly increases the risk of coronary heart disease (which leads to heart attack and stroke), especially along with other risk factors.

  High blood pressure can occur in children or adults, but it is more common among people over age 35.

- **Dyslipemia**: Elevated levels of serum lipids (dyslipemia and triglycerides) are extremely common. Epidemiological studies have shown that the level of total cholesterol in the blood is a strong predictor of the likelihood that an individual will develop coronary heart disease (CHD).

- **Cigarette Smoking**: It is the major contributor to CHD, stroke and peripheral vascular disease. It has been estimated that 30% to 40% of deaths of CHD each year can be attributed to smoking. Individuals who smoke, regardless of their level of other risk factors are at significant risk of premature CHD and death. Smokers, for example, have less of a chance of surviving a heart attack than nonsmokers.

- **Obesity**: Any level of overweight appears to increase CHD risk. Obesity can predispose the development of other risk factors, and the greater the degree of overweight, the greater the likelihood of developing other antecedents of atherosclerosis (such high blood pressure and diabetes) that will increase the probability that heart disease will develop. It also appears how the weight is distributed may be even more important than exactly how much a person weighs.

- **Diabetes Mellitus and Insulin Resistance**: Individuals with diabetes mellitus which occurs in adult life, have an increased incidence of CHD and stroke. Many individuals whose diabetes begins after age 40 or 50 (so-called adult-onset or Type II diabetes) often have higher than normal levels of insulin, which is an hormone responsible for maintaining blood sugar at normal levels. Some individuals do not respond as readily to insulin, and more is required. They have insulin resistance. Elevated levels of insulin can raise blood pressure and assist in the deposition of and reduce the removal of cholesterol from plaques in arteries.

- **Cocaine**: The use of cocaine has affects especially among the young adults poblation. Cocaine constricts the coronary arteries decreasing their blood flow to the heart and thus, reducing its oxygen supply. This can turn to abnormal heart rhythms, high blood pressure, cardiac crisis and even death.

In the group of risks that cannot be changed:

- **Age**: The risk of cardiovascular events increase as we get older. In many epidemiologic surveys, age remains one of the strongest predictors of disease. More than half of those who die of such attacks are over age 65.

- **Gender**: Men are more likely than women to develop CHD, stroke, and other cardiovascular diseases that are manifestations of atherosclerosis. Whether this is because male hormones -androgens- increase risk or because female hormones -estrogens- protect against atherosclerosis is not well understood. It is likely that both play a role, but that protective role of estrogens is the predominant factor.

- **Inheritance**: There is no question that some people have a significant grater likelihood of having a heart attack or stroke because they have inherited a tendency from their parents. In some instances, such as familial hypercholesterolemia (very high levels of cholesterol in the blood), the patter of inheritance is well understood and the specific biochemical defects are well characterized. For most cardiovascular risk factors, however, the specific way in which inheritance plays a role is not clear. As in almost situations in medicine, both heredity and environment play a role. Individuals with a story of AHD in the family simply have to be more vigilant if they wish to avoid heart attacks and strokes.

3.3 Cardiovascular Diseases

Atherosclerosis of the larger coronary arteries is the most common anatomic condition to diminish coronary blood flow. The branches of coronary arteries arising from the aortic root are distributed to the epicardial surface of the heart which, in turn, provide intramural branches leading to a structure known as *coronary tree* (Figure 3.b) and which is the responsible for the *myocardium* blood supply. Cardiovascular diseases are the straightforward consequence of the occlusion of these arteries, which is produced, as we have seen, by many factors. Depending on the severity of the artery occlusion, myocardial damages will be temporal causing myocardial ischemia or irreversible causing local necrosis of the muscle and even an Infarction.

3.3.1 Myocardial Ischemia

Ischemic Heart Disease (IHD) is a condition in which there is acute, intermittent, or permanent compromise in the oxygen supplied to the myocardium due to inadequate perfusion. This makes the myocardium not to fully contract, leading to a decrease of the cardiac output (rate blood flow resulting from heart pumping action). In addition ischemic myocardium is less compliant, 'stiff', making it less able to relax in response to blood entering in diastole phase and thus increasing chamber pressure which has adverse consequences on myocardial pulmonary function.

3.3.2 Myocardial Infarction

Myocardial infarction (MI) is a subset of myocardial ischemia in which there is a complete absence of oxygen supply and there is permanent damage to the myocardium. The term infarction describes necrosis or death of myocardial cells. The time between the onset of the ischemia and the muscle cell death is about 15 to 20 minutes in most cases. The left ventricle is the predominant site for infarction; however, right ventricular infarction occasionally coexists with infarction of the inferior wall of the ventricle. During acute myocardial infarction, the central area of necrosis is generally surrounded by an area of injury, which in turn is surrounded by an area of ischemia. Thus, various stages of myocardial damage coexist. The distinction between ischemia and necrosis is whether the phenomenon is reversible or not.

3.3.3 Heart Failure

Heart failure is a condition where the heart cannot pump enough blood throughout the body. Heart failure does not mean that the heart has stopped or is about to stop working. It means that the heart is not able to pump blood the way that it should. The heart cannot fill with enough blood or pump with enough force or both. Heart failure develops over time as the pumping action of the heart grows weaker.

It can affect the left side, the right side, or both sides of the heart. Most cases involve the left side where the heart cannot pump enough oxygen-rich blood to the rest of the body. With right-sided failure, the heart cannot effectively pump blood to the lungs where the blood picks up oxygen. The weakening of the pumping ability of the heart causes: Blood and fluid to "back up" into the lungs; the buildup of fluid in the feet, ankles, and legs; and finally tiredness and shortness of breath.

4 Medical Imaging Technology Overview

4.1 Introduction

If a CVD is detected in premature phases, there is the possibility of modifying some risky factors such as diet, weigh, smoking habits, physical exercise etc. and keep on a normal life. Nevertheless, when injury is in advanced stages this may be not enough. To provide a good diagnosis and plan an appropriate treatment, the extent and localization of the damage should be known. To this purpose there are several imaging techniques that have the ability of showing the anatomic structure and function of the heart.

When in 1895 Wilhelm Roentgen waved his hand through stream of X-rays and saw his bones silhouetted on a screen across the room, he began a new era in medicine: for the first time, physicians could see into the hidden recesses of the body. In the century following Roentgen's accidental discovery, X-ray was followed by a variety of different methods of imaging body tissues, such as ultrasound, nuclear medicine: single photon emission tomography (SPECT) and positron emission tomography (PET); angiography, computed tomography (CT) and magnetic resonance (MR). Regardless the method used, all of them are based on the physics of the interaction of energy and biological tissue.

All these imaging techniques can be divided in many groups according to some characteristics.

4.2 Ionizing vs Non-ionizing Radiation

A first division could be in those which use ionizing radiation (IR) versus those that do not. The IR group consists of those images created by the use of x-rays or γ rays. Both x-rays and γ rays are high energy, short wavelength electromagnetic radiation (e.g. 0.1 to 0.001 angstrom range) that is capable of penetrating and passing through most tissues. These radiation waves are created either by radioactive nuclear decay of tracer atoms injected into the body (nuclear medicine) or by x-ray tubes, which create their energy waves by bombarding a tungsten anode target with high energy [40 to 150 keV] electrons. Transducing these waves into light by a fluorescent screen, sodium iodide crystal, or by photon counters allows images (say, of differential tissue absorption - or of the radioactive atomic locations in the case of nuclear tracers) to be formed into an image on film or displayed on a cathode ray tube display.

Radiography, angiography, CT and nuclear scintigraphy belong to this group.

Non-ionizing radiation techniques mainly use either acoustic pulses (ultrasound) for echo-ranging imaging (somewhat like radar) or radio-waves combined with high-field magnets, in the case of magnetic resonance imaging.

4.3 Tomography vs Projection

Another division of image techniques is the following: tomographic or projection techniques. Projection techniques, such as x-ray films are "shadowgram-like" transilluminations of the body with a penetrating high energy ionizing radiation. The differential absorption of this radiation by the various tissues of the body creates on film an inverse shadow of the body. Less dense, lower atomic weight structures, such as the lung, allow transmission of more radiation flux producing greater fluorescence on an absorbing screen which exposes an adjacent film more densely, making those areas black. Higher atomic weight structures (bone) absorb and block the radiation, thus do not result in the exposure of the silver halide grains in the film emulsion, and so bony structures such as the ribs appear white (transparent). Because of the nature of trans-illumination, various tissues are imaged as overlapping each other (Figure 4.a .b)

and often need multiple views as, for instance, in angiography for visual under-standing. Radiography, angiography and planar scintigraphy belong to this group

Tomography (Figure 4.c) is a "slicing" of the body into various sections and in various view planes (and can be generated by x-rays in the case of computed tomography, or ultrasound in the case of echocardiography) and allow presentation of anatomy in a more readily understandable way because they avoid the confusion of overlapping structures. The tomographic sections when viewed in sequence or integrated by a computer allow the display and understanding of 3-dimensional anatomy.

MR, CT and echocardiography belong to this group.

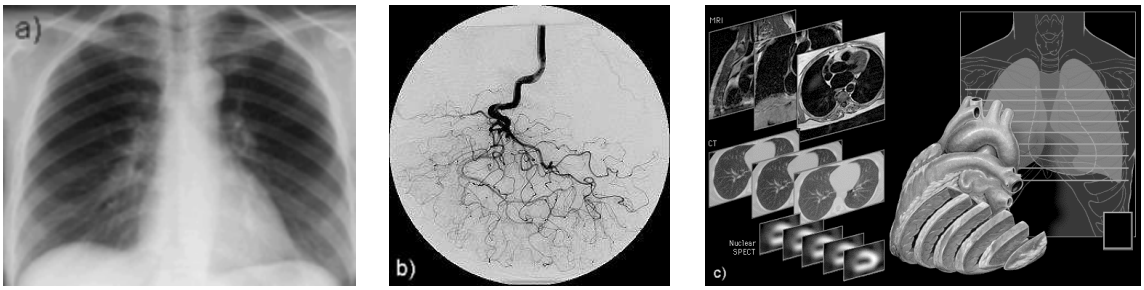

Figure 4: a) and b) X-ray radiography and Angiography. Two examples of projection techniques. Overlapping of structures are clearly appreciated. c) Tomographic scheme showing how anatomy is sliced.

4.4 Image Modalities

4.4.1 Coronary Angiography

Coronary angiography (Figure 4.b) is an X-ray examination of the blood vessels or chambers of the heart. A very small tube (catheter) is inserted into a blood vessel in the groin or arm. The tip of the tube is positioned either in the heart or at the beginning of the arteries supplying the heart, and a special fluid (called a contrast medium or dye) is injected. This fluid is visible by x-ray, and the pictures that are obtained are called angiograms. Often an angiogram is necessary before deciding whether coronary disease needs more treatment. Due to the fact that angiography returns a 2D projection of a naturally 3D structure (coronary vessel tree), more than one projection is required in order not to omit possible coronary lesions.

4.4.2 Computed Tomography

Computed tomography was developed in 1970's and it supposed a great revolution since in 1895 conventional x-ray images appeared. During the century the modality evolved but the underlying idea remained the same: the absorption of x-rays as they pass trough different parts of the body. One of its limitations was the inability to produce sectional information due to the impossibility to distinguish depth. CT resolved this problem. CT scanners produce multiple cross-sectional images of the body from which a 3D volume can be derived. The mathematical tool that allows for the image reconstruction from x-ray projections was created in 1917 by Radon, but was not until computers were fast and economic enough that it could be applied. Currently there exist more sophisticated CT scanners that supply straightforward 3D volumes in relatively short time.

In cardiac imaging respiratory and cardiac motion causes non-negligible artifacts that have to be compensated. A technique that tries to overcome these limitations is *single slice sequential* (transaxial). First of all the patient is asked to hold the breath so that first artifact disappears. After this the sequence acquisition is performed for each plane separately. The acquisition is triggered with the ECG although it

is sensitive to irregular heart beats and arrhythmias. The temporal resolution of this technique is 100ms and its main limitation is the difficulty to coverage the whole heart volume in just one breath hold. This last drawback can be overcome by *multislice sequential* (transaxial) imaging, which simultaneously acquires multiple slices at each position. This reduces considerably the aquisition time.

A final and inevitable drawback is the invasive character of this image modality. CT exposes the patient to harmful x-ray radiation. The exposure is greater than in a single x-ray radiography in the sense that CT combines information of several radiographs.

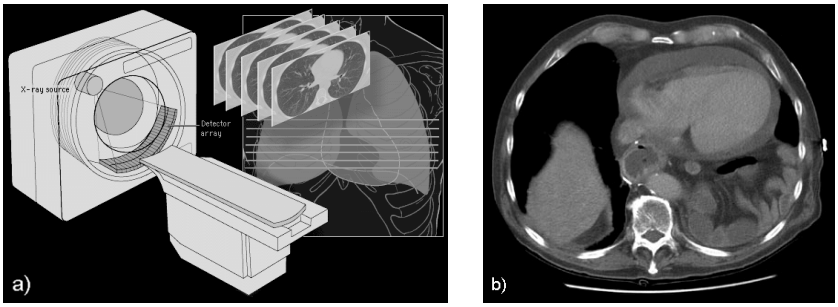

Figure 5: a) CT scanner device. b) Sectional CT image showing different organs.

4.4.3 Nuclear Medicine: PET and SPECT

Meanwhile CT provides anatomical information in addition, Nuclear Medicine (NM) or *radionuclide scanning*, provides information about the metabolic functions of the human body. To create these images, compounds like simple sugars (i.e. glucose) are labelled with signal-emitting tracers (radiopharmaceuticals) and are injected into the patient. A scanning machine records the signals these tracers emit as they journey through the human body and collect in the various organs targeted for examination. A computer reassembles the signals into images, resulting in pictures, which show functioning of the organs and tissues. The scan is made by slices, as in CT, so that 3D information is achieved. This is called *Emission Computed Tomography* (ECT). Other difference in respect to the CT is that this is based on energy attenuation, while ECT is based on energy radiation (Figure6.a).

The technique of ECT can be classified into two separate modalities: *Single-photon emission computed tomography* (SPECT) and *Positron emission tomography* (PET). SPECT uses radioisotopes where a single γ-ray is emitted per nuclear disintegration, while PET uses radioisotopes where two γ-rays are emitted simultaneously when a positron from nuclear disintegration annihilates in tissue.

In cardiac imaging, PET is a very useful tool for myocardial perfusion assessment, i.e., the blood flow (Figure6.b and .c). It shows the parts of the muscle that have been affected by an ischemia or an infarction and the extent of it so the patient can be given the appropriate treatment.

Despite the great potential of NM, it has several disadvantages. The first one is its poor spatial resolution. For this reason there is a considerable interest in combining NM with other image modalities that provides good spatial resolution. PET/CT is an instance of it. Other drawback is the hazardous character of NM. Despite radiopharmaceuticals are designed to fulfill several safety conditions such that natural clearance process must remove them in a short time, in practice isotopes used in PET imaging do not completely meet them.

4.4.4 Ultrasound Imaging

The use of ultrasound in medical imaging started in the 1950's. During that decade, advances in technology made it possible and ultrasound became a medical tool for diagnosis. Ultrasound refers to sound

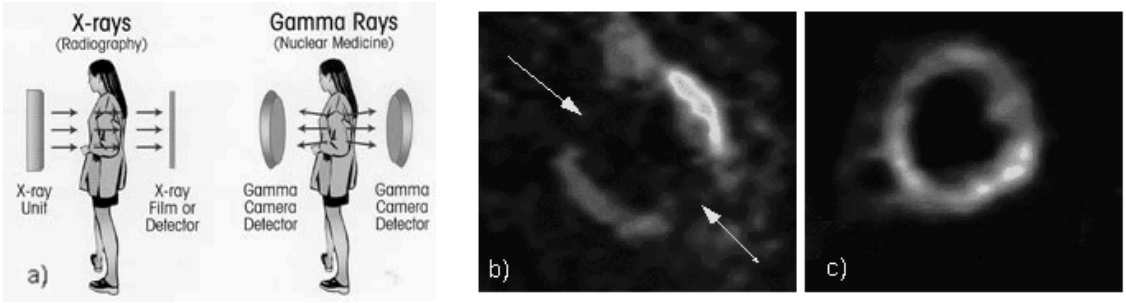

Figure 6: a) Energy absorption in CT and energy emission in NM. b) Image of heart which has had a myocardial infarction (heart attack). The arrow points to areas that have been damaged by the attack, indicating "dead" myocardial tissue. c) Normal heart.

waves of frequencies above 20 KHz which humans cannot perceive. Nevertheless, for medical, applications frequencies must lie between 500 KHz and 30 MHz. This kind of images are based on ultrasound emission pulses and posterior reception of their echoes when interacting with internal structures of the body. The processing of the echoes generate the image. Ultrasound imaging techniques are very attractive due to the fact that they provide real time sequences using compact equipment the price of which is relatively small compared to other imaging techniques. And moreover, it is a non-invasive technique.

The most common ultrasound device consists of a transducer that is placed against patient skin surface, and as close as possible to the organ to be seen. Between the skin and the transducer a sound wave conductor gel is applied in order to reduce external noise. Nevertheless, there are other ultrasound devices. It is worth mentioning *intravascular ultrasound* (IVUS). Transcatheter IVUS imaging is a technique in which a miniaturized ultrasound transducer, mounted on the tip of catheter, is inserted directly into an artery or vein to produce unique images of the composition of the vessel in detail to evaluate atherosclerotic plaque deposits and obtain information of vessel lumen etc. However, the lack of third dimension to provide more details on the exact position and orientation of these planes makes difficult the task of reconstructing with accuracy the architecture of the vessel and the morphology of the plaque. To overcome this limitation, IVUS/angiography fusion is an interesting technique that must be taken into account.

There is an interesting property of sound. When the signal reflects to moving structures, like moving cells, the original signal undergoes a detectable change in frequency that is called the Doppler effect. This effect also occurs when the transducer is moving and the tissue remains still or when the interface is moving and the transducer is stationary. This property is of importance because, among others, it allows the visualization of myocardial perfusion. Due to the fact that red cells are too small, echocontrast agents made of microbubbles that act as echopotentiators are injected to the patient in order to enhance visualization. This technique called *Contrast Echocardiography*, contrary to PET, is non-invasive and, meanwhile few hospitals posses PET scanners, ultrasound equipment is available almost everywhere.

An important limitation of the ultrasound imaging is that the quality of images is very poor. Spatial resolution rang goes from 1-3 mm or 2-5 mm depending on the method used and it is very sensitive to noise giving echographic images a typical speckles appearance.

4.4.5 Magnetic Resonance

Magnetic resonance imaging (Figure 8.c) depends on immersing the body in a steady, strong magnetic field, commonly up to 1.5 Tesla (i.e. 15,000 Gauss for reference, the earth's magnetic field is about 0.5 Gauss). Some modern "whole-body" (i.e. apertures wide enough to accept a person's thorax) machines now operate at 4 or more Tesla. Hydrogen atoms, pervasive in the water which makes up about 70% of the body's mass, have a dipole property by virtue of their characteristic spins. These spinning atoms,

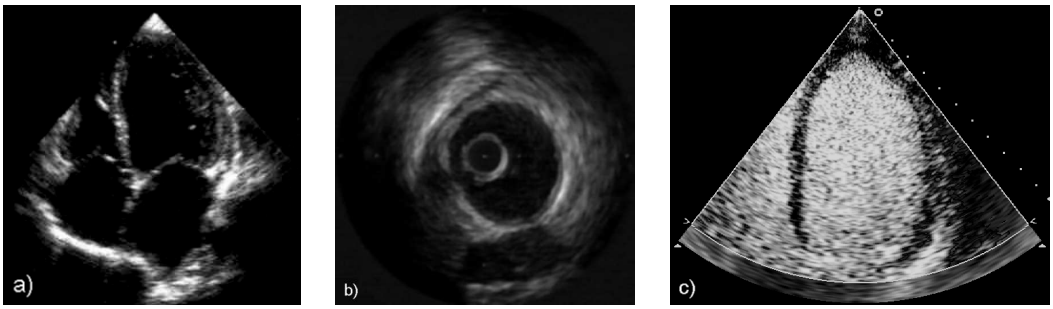

Figure 7: a) Echocardiography. Long axis view of the heart. b) IVUS section showing inner vessel morphology. c) Contrast echocardiography showing myocardium perfusion.

influenced by the permeating magnetic field, precess like a top and a slight majority of hydrogen atoms precess in alignment with the dominant magnetic field. Subjecting the body tissues to an additional magnetic field gradient to prepare a specific tissue slice of the body for imaging while adding a precisely tuned radio frequency pulse permits these specially prepared hydrogen atoms to absorb this radiation in a resonant fashion. Hydrogen atoms, by virtue of their surrounding magnetic environment and their excited state, alter their net magnetic axis direction temporarily. This excited state rapidly decays to a lower energy state while emitting its own unique radio frequency signal which can be detected by an external radio-frequency coil. From these signals there are mathematical methods, as mentioned in CT, for calculating tissue-related images.

Special pulse-echo sequences permit high level signals to be detected from flowing blood, therefore images can be created of the vasculature and its blood velocity characteristics. So-called "functional MRI" detect differences oxygen-saturated and de-saturated blood. Thus brain processes of "thought" such as vision, motor control and speech can be detected (though at low spatial resolution) by virtue of their local oxygen consumption when activated.

Recently a new imaging technique based on MR principles have been developed. It is called Tagged MRI (Figure 8.b) and it marks the myocardial tissue by applying a sequence of radio-frequency pulses to pre-saturate thin planes of the myocardium prior to the imaging. These "tags" persist in the myocardium through the heart cycle and deform by the underlying movement of the heart. This technique allows every myocardial point to be tracked. This technique is very valuable due to the fact that the myocardium is a very uniform tissue and the lack of identifiable marks makes point tracking an impossible task for the rest of imaging techniques.

4.5 Discussion

As we have seen, there are multiple medical imaging techniques that can be used in order to assess CVD, nevertheless not all of them will be always used. There are many criterions for the choice of one technique or another. Amongst them there are issues such, equipment cost and thus availability of the equipment in an hospital, or invasiveness of the technique (ionizing or not). Echography has arised as one of the most used imaging techniques, due to its cost/image quality/versatility ratio despite CT and MR scanners are also quite extended. NM are the least widespread imaging techniques.

Currently the trend in medical imaging points to multimodality image fusion. It involves combining the power of different imaging techniques to enhance the final result and obtain better diagnostics. In this sense we mention PET/CT fusion, which mixes the functional information given by PET and the spatial resolution given by CT. Another fusion technique involves IVUS with angiography. The method overcomes the lack spatial information presented by IVUS and the lack of morphological information of the artery presented by angiographies.

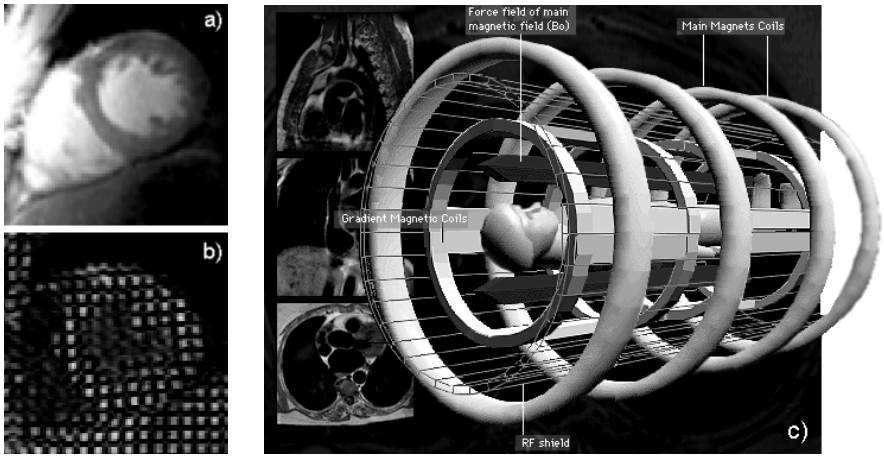

Figure 8: a) Myocardium seen in an ordinary MR image. Uniformity of the tissue and the lack of landmarks is well appreciated. b) Tags printed over the myocardium provided by MR tagging. c) MR Scanner device.

4.6 Developed Projects in Medical Imaging

We have been working in two medical imaging projects. The imaging modalities involved were Contrast Echcardiography and SPAMM tagged MRI. To them we applied the segmentation framework that we have developed and that we expose in further sections, to extract structural and quantitative information.

4.6.1 Contrast Echocardiography

To asses the severity of cardiovascular diseases, often it is of importance to analyze the blood flow supplied to the myocardium. This is called myocardial perfusion. Due to the fact that LV performs the most energy-consuming function of the heart, the oxygen delivery to the whole body, it would be interesting to quantify its blood perfusion as it can be decreased up to three or four times if there is an obstruction of the epicardial or intramyocardial arteries (Figure 3.b).

The most widespread image techniques for myocardial perfusion analysis are SPECT, PET and MR. Although they give high quality information about myocardial perfusion they are not widely available in most hospitals because of their cost. Moreover, SPECT and PET use ionizing radiation, as we have seen in section 4.2, which makes them invasive to the patient. The availability, low cost and non-invasiveness of echocardiography, in addition to great progresses in microbubble contrast agents during last decade, have projected the contrast echocardiography [44] as a powerful tool in the myocardial assessment. These microbubbles, act as echoenhancers of sound amplifying the reflected waves and thus enhancing the resulting image.

However, it is difficult to get conclusions directly from images. Quantitative parameters must be extracted to interpret the sequence of perfusion images. This is done by tracking myocardial points along the cardiac cycle meanwhile the process of destroying the microbubbles (using a high energy pulse) and reperfusing again is repeated ([78], [79]).

4.6.2 SPAMM Tagged MRI

Magnetic Resonance is one of the most common, non-invasive, cardiac imaging techniques as it can provide into a single sequence examination, information about anatomy, structure, global and regional function and contraction of the heart. Nevertheless, the lack of identifiable landmarks within the myocardium (Figure 8.a) makes motion assessment limited due to the fact that many patients may have

significant regional dysfunction while maintaining an ejection fraction relatively within normal limits. To overcome this limitation, a new image modality is designed: Tagged Magnetic Resonance (TMR) ([55], [56], [57]) (Figure 8.b), which uses a special pulse sequence to spatially modulate the longitudinal magnetization of the subject prior to acquiring image data. This is called SPAMM and produces a grid over the myocardium, which deforms by the underlying motion of the heart. Thus, inner tissue deformation becomes visible.

Despite the potential of this imaging technique, MR tagging has not been established as a standard clinical tool though it is very used in research. Results from MR tagging have been found to agree well with echocardiographic data, [54]. It also has been proven that tagging enables accurate measurement for diseases such as *hypetrophic cardiomyopathy* (HCM), *arteriosclerosis* and to better understand the correlation of coronary artery disease with myocardial motion abnormalities.

5 Medical Imaging Analysis

5.1 Introduction

The role of medical imaging has expanded beyond simple visualization of anatomic structures due to its rapid development and proliferation. It has become a tool for surgical planning and simulation, intra-operative navigation and diseases progress tracking. Also quantitative data derived from images has become a valuable method to asses the severity of a particular disease and compare it to other solved (or non-solved) cases. Computer assistance is thus required to extract relevant information amongst the great amount of data returned by image devices. This process should be done in as minimal time as possible because in some cases time could mean to save a life or not. In addition we cannot expect a radiologist to spend many hours in front of a computer postprocessing and analyzing endless raw image sequences because accurate and repeatable data must be extracted without inter or intra-observer variability addition. For this reason automatic or at least, minimal-human-interaction postprocessing methods must be tailored for each particular problem.

The main issue in medical image analysis is to analyze anatomic structures of the body, for this reason the main task given an image, is to separate them from other non-interesting parts of the image. This is known as *segmentation* and is the process by which a point is labelled as belonging to the structure of interest or not. In computer vision there are many segmentation techniques. Basic segmentation techniques such as thresholding, watersheds, edge-detectors like *sobel*, *prewitt* or *canny* and ridge and valley dettectors are not well suited due to noise and other artifacts that may cause incorrect regions and boundary discontinuities.

Deformable models offer a unique and powerful approach to image analysis that combines geometry, physics and approximation theory. They are well suited in segmenting and tracking anatomic structures by exploiting (bottom -up) constraints derived from the image data together with (top-down) *a priori* knowledge about the location, size, and shape of these structures. The inherent continuity and smoothness of the models can compensate for noise, gaps and other irregularities in object boundaries.

Deformable models were first proposed for computer vision and computer graphics in the mid 1980's by Terzopoulos *et al.* in [1]. He also introduced the theory of continuous (multidimensional) deformable models in Lagrangian dynamics setting [2], based on deformation energies in the form of generalized splines (controlled continuity) [3]. *Deformable contour models*, a particular case of deformable models, were introduced in [4] and became very popular under the name of *snakes*. Snakes are planar parametrized curves that are used to approximate shapes of object boundaries in images, assuming that curves are piecewise continuous or smooth. These kind of deformable models are also known as *parametric deformable models*.

5.2 Active Contour Models

Formally, a snake is represented by $v(s) = \{(x(s), y(s)\} \in \mathbb{R}^2$, where $x(s)$ and $y(s)$ are spatial coordinate functions and $s \in [0, 1]$ is the parametric domain; that tries to minimize its energy $\mathcal{E}_{snk}$ which is, in turn, a composition of two other energies: internal and external

$$\mathcal{E}_{snk}(v) = \mathcal{E}_{int}(v) + \mathcal{E}_{ext}(v). \tag{1}$$

Internal energy imposes constraints about curve smoothes and flexibility

$$\mathcal{E}_{int}(v) = \int_0^1 \alpha(s)\|\frac{\partial v}{\partial s}\|^2 + \beta(s)\|\frac{\partial^2 v}{\partial^2 s}\|^2 ds, \tag{2}$$

while external energy attracts the curve towards image main features (boundaries in image segmentation)

$$\mathcal{E}_{ext}(v) = \int_0^1 \mathrm{P}(v(s))ds. \tag{3}$$

In this equation P(x, y) denotes a scalar potential function specially constructed from image so that local minima coincide with intensity extrema, edges, and other features of interest. There are many ways to create a potential, the original idea found in [4] proposes

$$\mathrm{P}(x, y) = -|\nabla(\mathrm{G}(x, y) * \mathrm{I}(x, y)|^2, \tag{4}$$

where $\mathrm{I}(x, y)$ is the image and $\mathrm{G}(x, y)$ is the gaussian filter. Nevertheless it is known that this is not the best way to define the potential and proposes to use contours found by an edge detector (canny for instance) and to propagate them by using a gaussian filter to smooth. Another way to construct more robust potential fields is using distance maps or even functions of them

$$\mathrm{P}(x, y) = d(x, y); \qquad \mathrm{P}(x, y) = -e^{-d(x,y)^2} \tag{5}$$

where $d(x, y)$ represents the distance between (x, y) and the nearest point over the contour. This potential defines a metric so that at each point distance from contours is known, nevertheless more information about the nearest contour would valuable in order to properly drive the snake. This is what is proposed in [5], where gradient direction of contours are also propagated. Depending on the potential that is synthesized, and thus the external forces, snakes's behavior will vary leading to different segmentation results.
In accordance with the calculus of variations, the contour $v(s)$ which minimizes the energy (1) must satisfy the Euler-Lagrange equation

$$-\frac{\partial}{\partial s}(\alpha(s)\frac{\partial v}{\partial s}) + \frac{\partial^2}{\partial s^2}(\beta(s)\frac{\partial^2 v}{\partial^2 s}) + \nabla \mathrm{P}(v(s)) = 0 \tag{6}$$

This vector-valued PDE expresses the balance of internal and external forces when the contour rests in equilibrium. The first two terms represent the internal stretching and bending forces respectively, while the third term represents the external forces that couple the snake to image data.

In many medical imaging applications, structures evolve in time. Heart is an example of it. Thus, extending the above formulation such that incorporates dynamic information to segment is of great

interest. This can be done by considering an evolving contour $v(s) = \{(x(s,t), y(s,t)\} \in \mathbb{R}^2$ where $t \in [0, \infty]$. Solution (6) is thus extended to

$$\mu \frac{\partial^2 v}{\partial t^2} + \gamma \frac{\partial v}{\partial t} - \frac{\partial}{\partial s}(\alpha(s)\frac{\partial v}{\partial s}) + \frac{\partial^2}{\partial s^2}(\beta(s)\frac{\partial^2 v}{\partial^2 s}) = -\nabla \mathrm{P}(v(s)) \tag{7}$$

The first two terms on the left hand side of this PDE represent inertial and damping forces. Equilibrium is achieved when the internal forces balance and the contour comes to rest, i.e., $\partial v/\partial t = \partial^2 v/\partial t^2 = 0$, which yields the equilibrium condition (6). To solve (6) and (7), numerical methods have to be applied.

5.3 Deformable Models in Medical Imaging

The underlying idea of snakes is the same for all the parametric deformable models. Following works have also been applied to medical imaging analysis: [6], [7], [8], [9], [11], [10], [12]. In them, users can use the interactive capabilities of these models and manually fine-tune them and, when the contour is fitted, it can be used as initial boundary approximation for neighboring slices in tomographic images and the resulting contours can be connected to form a continuous 3D surface model ([13],[14], [11], [10], [7]). This idea is the same for tracking structures in 2D image sequences, where the final segmentation in one frame becomes the initialization of the active contour in the next. This way, the method becomes faster.

5.4 Shortcomings of Deformable Models

The application of snakes and other similar deformable contour models to extract regions of interest (segmentation) is, however, not without limitations. First of all, snakes have to be initialized close enough to the boundary of interest in order to get influenced by its potential (external) forces, and avoiding them to fall into wrong local minima, i.e., get trapped by the forces of wrong (spurious) boundaries (shape degeneration). Thus to initialize the snake is certainly a problem that have to be carefully treated.
Another drawback is the election of the elasticity parameters α and β. A compromise have to be reached so that these parameters ensure smooth properties of the snake while allowing it to fit boundaries with high curvature.
Topologically, snakes are not well resolved. They are not able to change their topology, an interesting property that would be desirable in many medical imaging applications.
There are other issues as convergence, numerical stability or computational cost which are more related to the numerical implementation of the snakes.

Various methods have been proposed to improve the above limitations and to fully automatizate segmentation process. For instance [11] and [10] use an "inflation" force that expands the snake beyond spurious edges making it fall into strong boundaries. It also makes the final result less sensitive to the initialization procedure. These kind of "inflation" forces were introduced in [1].
In order to reach global solution, [15] use dynamic programming to perform a more extensive search for global minima. [16] and [17] minimize the energy of active contour models using a simulated annealing which is known to give global solutions and allow the incorporation of non-differentiable constraints.
In [16], [18], [19], [20], [21] and [22], the use of discriminant functions is proposed in order to incorporate region based features. Discriminant function allows the inclusion of additional image features in the segmentation and serves as a constraint for global segmentation consistency. The result is a more robust energy functional and a much better tolerance to deviation of the initial guess from the true boundaries. Sensitivity to insignificant edges is decreased.
Recently, several works ([23], [24], [25], [26], [27]) have been developing topology independent shape modelling schemes that allow a deformable contour or surface model to not only represent long tube-like shapes or shapes with bifurcations, but also dynamically change its topology when required. This

kind of deformable models, are known as *geodesic deformable models*. They are based on active contours evolving in time according to intrinsic geometric measures of the image. The evolving contours naturally split and merge, allowing the simultaneous detection of several objects and both interior and exterior boundaries. The proposed approach is based on the relation between active contours and the computation of geodesics or minimal distance curves. The minimal distance curve lays in a Riemannian space whose metric is defined by the image content. This geodesic approach for object segmentation allows to connect classical "snakes" based on energy minimization and geometric active contours based on the theory of curve evolution.

5.5 Incorporating A Priori Knowledge

Despite deformable models are well suited in medical analysis, their formulation is too general and often they are not enough to obtain the desired results. The structures to be segmented are quite complex and not always completely visible but partial. Nevertheless they are present and despite between subjects certain variability is appreciated, we beforehand know approximately the shape we are looking for, its size, orientation etc. It would be desirable to incorporate as many a priori information into our deformable model as possible, in order to obtain a more robust method able to find out the structure of interest, even in the worst conditions.

A first instance of deformable models that incorporate a priori knowledge about shape, are those based on superquadrics. Superquadrics contain a small number of intuitive global shape parameters that can be tailored to the average shape of a target anatomic structure. Furthermore, the global parameters can often be coupled with local shape parameters such as splines resulting in a powerful shape representation scheme thus, while global parameters efficiently capture the gross shape features of the data, the local deformation parameters reconstruct the fine details of complex shapes ([28], [29], [30], [31]).

Another interesting way to add a priori knowledge about shape ([32], [33], [34], [35]), is by capturing the statistics of shapes in a training set. Special landmarks (always the same) are manually marked for each image. A *point distribution model* is constructed by applying a PCA to this data thus, all "allowable" shapes are generated by using the mean shape and a weighted sum of the major modes of variation. Object boundaries are then segmented using this point distribution model by examining a region around each model point to calculate the displacement required to move it towards the boundary. These displacements are then used to update the shape parameter weights.

5.6 Discussion

We have mentioned multiple segmentation methods all of them in the field of deformable model techniques. Each of them trying to solve any limitation presented by its predecessors. Nevertheless, none of them can be chosen as the optimal medical imaging segmentation method. There are two basic factors to have into account when choosing a particular method:

- Depending on the shape complexity (topology, curvature etc.) of the target structure to be segmented, a method or another will be required.
- Quality of images will strongly depend on the device used to obtain them (CT, MR, Echography). Some devices will present artifacts that will require sophisticated segmentation methods to overcome them.

Certainly it would be desirable for a method to be capable to deal with all structures and all kind of images, but the reality points that segmentation methods must be tailored for every problem in particular.

Another desirable property that segmentation methods should present is the completely automated interpretation of medical images. This would increase the speed, accuracy, consistency and reproducibility of the analysis. However, the interactive or semiautomatic methodology is likely to remain dominant

in practice for some time to come, especially in applications where erroneous interpretations are unacceptable.

6 Generalized Active Shape Models (GASM)

6.1 Introduction

If we think of natural objects, a banana for instance, we will describe it, more or less, as a yellow curved narrow ellipsoid, whose length goes between 10 and 25 cm approximately. This general description of a banana, certainly embeds the whole range of banana shape variability (the color, for our purpose, is meaningless). Having this in mind, a good approach in describing objects, is to represent them as constrained variations applied to a golden object. In this section we introduce a method to create compact models from a set of significant examples that can represent both: shape and allowable variability, by extracting statistical information from the distribution and the relation between labelled points that represent the target structure.

In the previous section we have reviewed many segmentation methods in the framework of the deformable models. Those that incorporate a priori knowledge embed into a flexible model, seem to be the most suited for medical imaging analysis. Thus, if we are able to incorporate the shape model above mentioned to the deformable model, we will get a powerful segmentation tool.

6.2 Point Distribution Models (PDM)

In order to obtain a model that represents the shape variation of a certain structure or object, a point distribution model (PDM), the first step is to assemble a training set of images that recovers the shape range in which the particular structure or object can vary [35].

Once the training set is constructed, is the turn for the most important (and time-consuming) step of the process: the point labelling of the training set. This is given an image, to label points over its boundary. It is worth mentioning that the contour represented by such points do not have to be connected due to the fact that the construction of the model just takes into account the global spatial relations between points regardless which part of structure they belong to and if they are connected (Figure 9 (a), (b)).

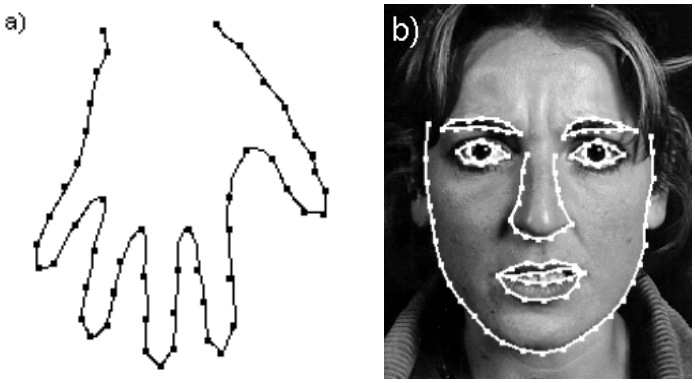

Figure 9: Point labelling in a connected boundary, a), and in an unconnected boundary b).

Care must be taken when labelling points because each of them represents a particular part of the structure that has to be preserved along the set. For instance, Figure 10.a shows an image of a printed circuit board in which a PDM of transistors have to be derived. Figure 10.b show the points that will be labelled. In this model, for instance, points $\{0, 31\}$ always represent one end of the wire, meanwhile

points $\{5, 6, 7, 8, 9, 10\}$ represent a side of the resistor's body and so on. Finally in Figure 10.c we can appreciate shapes extracted from the training set, following the labelling point criterion.

Given the ith image in a training set composed of N instances, we will represent the ith shape as an ordered set of M points. No matter which order criterion is used, though chosen one it must be respected. The most common representations are:

$$X^i = [x_1^i, y_1^i, x_2^i, y_2^i, \ldots, x_M^i, y_M^i]^T; \quad i \in 1, \ldots, N \tag{8}$$

or equivalently:

$$X^i = [x_1^i, x_2^i, \ldots, x_M^i, y_1^i, y_2^i, \ldots, y_M^i]^T; \quad i \in 1, \ldots, N \tag{9}$$

These raw representation of the shapes is still not prepared to extract meaningful data, and have to be aligned in a common coordinate system. This process is known as shape alignment.

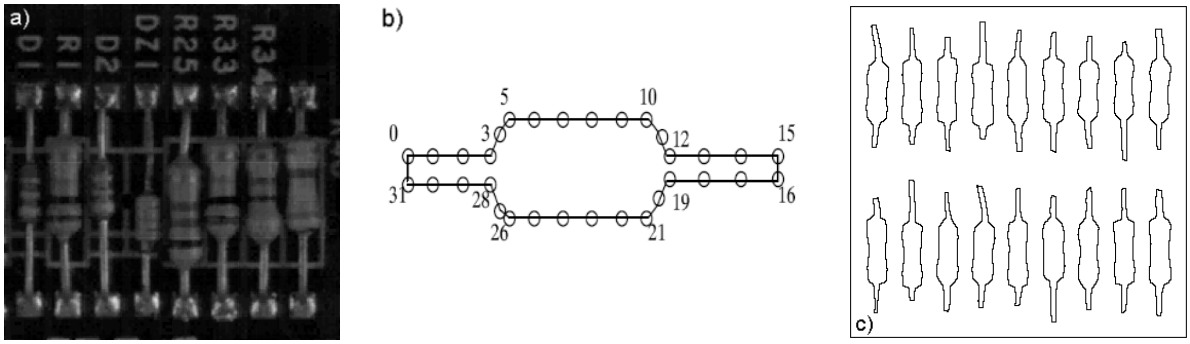

Figure 10: a) Image of a printed circuit board showing examples of resistors. b) Ordered set of labelled points in a shape. c) Examples of resistor shapes from a training set.

6.2.1 Aligning the Shapes

The modelling method works by examining the statistics of the coordinates of the labelled points over the training set. Before this, a process of alignment of the shapes must be done in order to remove similarities between shapes, i.e., rotation, scaling and translation artifacts. This way we will be able to capture information about the intrinsic shape variation between the examples in the training set.

We will first consider the problem of aligning two shapes X^i and X^j, by finding the least squares solution of the following expression:

$$E^{ij} = \|X^i - M(X^j)\|_2^2 \tag{10}$$

i.e., the parameters of M that minimize 10, where M is a similarity that rotates by θ, scales by s and translates by $t = (t_x, t_y)$ the points of the jth shape X^j as:

$$M \begin{pmatrix} x_k^j \\ y_k^j \end{pmatrix} = \begin{pmatrix} (s\cos(\theta))x_k^j - (s\sin(\theta))y_k^j + t_x \\ (s\sin(\theta))x_k^j + (s\cos(\theta))y_k^j + t_y \end{pmatrix} \tag{11}$$

If we translate the centroids of the shapes to the origin, we can assume that $t_x = t_y = 0$. Finally if we set $a = s\cos(\theta)$ and $b = s\sin(\theta)$, the solution that minimizes (10) is given by [43]:

$$a = \frac{\sum_{k=1}^{M}(x_k^i x_k^j + y_k^i y_k^j)}{\sum_{k=1}^{M}({x_k^j}^2 + {y_k^j}^2)} \qquad b = \frac{\sum_{k=1}^{M}(x_k^i y_k^j + x_k^i y_k^j)}{\sum_{k=1}^{M}({x_k^j}^2 + {y_k^j}^2)} \tag{12}$$

We have seen how to align two shapes. The iterative procedure used to align a set of shapes to a common frame of reference is known as Procrustes Analysis. It works by minimizing the distance to a computed (at each step) mean shape. Thus, given the shapes extracted from the training set $\{X^i\}_{i=1}^N$ the procedure to align them is described as follows:

1. Translate the centroid of each shape to the origin.
2. Arbitrarily choose a shape in the training shape set as the mean shape, $\bar{X}$.
3. Using equations (12), align each shape X^i to $\bar{X}$ by applying to every point the following transformation

$$\begin{pmatrix} \hat{x}_k^i \\ \hat{y}_k^i \end{pmatrix} = \begin{pmatrix} a & -b \\ b & a \end{pmatrix} \begin{pmatrix} x_k^i \\ y_k^i \end{pmatrix} \tag{13}$$

4. Calculate the mean of the aligned shapes:

$$\bar{X} = \sum_{i=1}^{N} \hat{X}^i \tag{14}$$

5. Go to step 3 until convergence.

6.2.2 Modelling Shape Variations

Now that all the shapes are aligned, we can think of their mean shape as the golden or idealized shape that represents the class of the target structure (remember the golden banana). Now shape variation has to be measured. A common technique that allows this measurement is the Principal Component Analysis (PCA), which transforms a set of correlated samples into a lower-dimensional set of uncorrelated samples. Let $\{\hat{X}\}_{i=1}^N$ be the set of aligned shapes, we can imagine every $\hat{X}^i \in \mathbb{R}^{2N}$ obtaining thus, a cloud of points in this space. What PCA does, is to find a new lower-dimensional orthogonal axis centered in $\bar{X}$ that follow the directions of higher variance. Each axis is known as principal component or principal mode of variation of the cloud. Now, any point $X \in \mathbb{R}^{2N}$ can be represented in this new P-dimensional space ($P < 2N$), by projecting it to the new axis (Figure 11).

The procedure for computing PCA is as follows:

1. The center of mass of the shape cloud is computed. In our case this is the last mean shape computed using equation (14) before convergence was reached in the alignment iterative method.
2. The correlation between individual shape elements is computed by calculating the covariance matrix, C:

$$C = \frac{1}{N}\sum_{i=1}^{N}(X^i - \bar{X})(X^i - \bar{X})^T \tag{15}$$

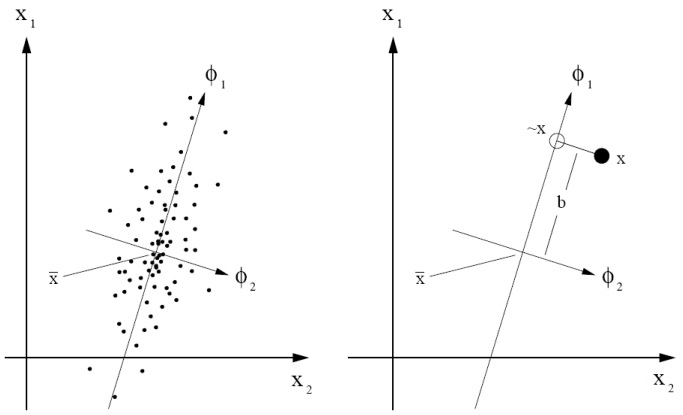

Figure 11: A simple visual depiction of PCA applied to a set of 2D points clustered around $\bar{X}$, which creates a set of principal components ϕ_1 and ϕ_2. Any point X can be approximated by the main component which codifies most of the information meanwhile information provided by ϕ_2 is underestimated.

3. The modes of variation, the ways in which the points of the shape tend to move together, are described by the unit eigenvectors of C, Φ_i of eigenvalue λ_i:

$$C\Phi_i = \lambda_i \Phi_i \tag{16}$$

and

$$\Phi_i^T \Phi_i = Id \tag{17}$$

which means that the eigenvectors are orthonormal. By convention we assume that $\lambda_i \geq \lambda_{i+1} \quad \forall i \in \{1, \ldots, 2N\}$. It can be shown that the eigenvectors of the covariance matrix corresponding to the largest eigenvalues, describe the most significant modes of variation in the variables used to derive the covariance matrix, and that the proportion of the total variance explained by each eigenvector is equal corresponding to the eigenvalue.

The ith eigenvector affects the kth point in the PDM by moving it along a vector parallel to $v_k^i = (dx_k^i, dy_k^i)$, where $dX^i = X^i - \bar{X}$ and which is obtained from the kth pair of elements in Φ_i

4. Most variation can usually be explained by a small number of, P, modes. A method for calculating P is to choose the smallest number of modes such that the sum of the variance explained is sufficiently large in respect to λ_T, where

$$\lambda_T = \sum_{i=1}^{2N} \lambda_i \tag{18}$$

Thus, the number of modes have to be chosen so that they can explain most of the shape variation observed in the training set.

5. Having computed $\bar{X}$ and Φ, any point $X \in \mathbb{R}^{2N}$ can be expressed in the new coordinate system as:

$$X = \bar{X} + \Phi b \tag{19}$$

where

$$b = \Phi^T (X - \bar{X}) \tag{20}$$

Nevertheless we reach the dimensionality reduction by choosing an appropriate number of variation modes, P for instance, that sufficiently explains the shape variation, thus any point in $\mathbb{R}^{2N}$ will now be approximated (projected) in this reduced space $\mathbb{R}^P$ by

$$X \approx \bar{X} + \Phi_P b_P \tag{21}$$

where

$$b_P = \Phi_P^T (X - \bar{X}) \tag{22}$$

and

$$\Phi_P = (\phi_1 | \phi_2 | \dots \phi_P) \qquad b_P = (b_1, b_2, \dots, b_P)^T \tag{23}$$

We have seen a method that given a set of shape samples, the training set, allow us to build a compact model of shape and allowable variation. This PDM determines a way to obtain valid shapes by varying the shape parameter b_P among a valid range: given its ith component, b_{Pi}, it is constrained to $-3\sqrt{\lambda_i} \leq b_{Pi} \leq 3\sqrt{\lambda_i}$. this is due to the fact that PCA assumes that the initial data cloud is a single cluster with an independent gaussian distribution along each principal component axis. Thus, given any (aligned) shape $\hat{X} \in \mathbb{R}^{2N}$, we can find the valid shape most similar to it by projecting the point into the new axes to find the valid shape parameter as in (22), and then, we generate the valid form, using (21).

As we previously told, it would be interesting to add the PDM, to a deformable model in order to perform a 'smart' segmentation.

6.3 Active Shape Models (ASM)

Active Shape Models (ASM) is a method created by Cootes *et al* [34], that incorporates shape information using the PDM above mentioned (a priori knowledge) to perform a more robust segmentation.

The steps followed by this algorithm are:

1. Suppose that we have previously created the PDM that recovers the shape variability of the class of the target structure. A first step consists of placing the class representant, i.e. the mean shape, close enough to the solution (we mentioned in the previous section that this is a problem that have to be treated separately and particularly for each problem). Due to the fact that the coordinate system of the training set and the one of the input image are different, we will have to apply a similarity to the mean shape. This is a composition of translation, rotation and scaling. Let $[M^0_{\theta,r,T}]^{-1}$ be this similarity, we initialize the shape as $X^1 = [M^0_{\theta,r,T}]^{-1}(\bar{X})$

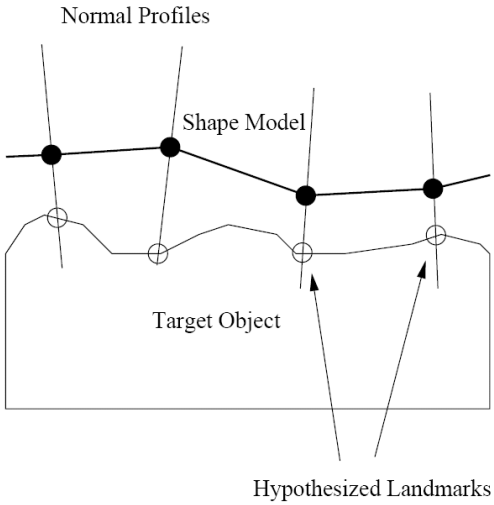

Figure 12: Strong edges search by every point in the shape model along their normal profile.

2. Given the ith shape X^i, for each labelled point in the shape boundary (x_k^i, y_k^i), a new position for it is searched. This is done along a perpendicular segment to the boundary that passes through this point. See Figure 12. This gives us an hypothesized shape which have to be supervised, i.e., to be said if it is a valid shape (those represented in our PDM) or not. And if not, to find the most similar valid shape.

3. X^i is aligned to $\bar{X}$ so that they share coordinate system and comparisons between them can be performed. Let $M_{\theta,r,T}^i$ be this the alignment transformation, $\hat{X}^i = M_{\theta,r,T}^i X^i \in \mathbb{R}^{2N}$ is calculated.

4. The most similar valid shape to $\hat{X}^i$ is obtained by projecting this shape to the new axes obtained by the PCA as in (22): $b^i = \Phi_P^T(\hat{X}^i - \bar{X})$ and thus,

$$\tilde{X}^i = \bar{X} + \Phi_P^T b^i \tag{24}$$

5. Finally the step of disaligning the allowed shape is performed. This is done by applying the inverse similarity obtained before:

$$X^{i+1} = [M_{T,r,\theta}^i]^{-1} \tilde{X}^i \tag{25}$$

6. Go to step 2 and repeat the process until convergence is reached.

6.4 Extending ASM: GASM

Clearly ASM is robust method well suited for medical imaging segmentation in the sense that has incorporated a priori knowledge about the shape of the structure that must be segmented. Nevertheless there is a weak point left in this method. It is the way that labelled points of the shape hypothesize their next position. They are constrained to search for strong edges along a normal segment and this,

often will not be enough to reach a desirable result. Some improvements have been performed in [33], where grey level appearance in a neighborhood of each labelled point is learned.

and nevertheless they remain analyzing along a normal segment. If we analyze what ASM does, we realize that, in fact, ASM is a recurrent combination of two main step, namely:

- **Prediction Step:** Each point in the structure boundary hypothesizes a new position along a normal segment according to some criterion. This step, as we have mentioned, is the weak point of the method and the one prone to be improved.

- **Regularization Step:** A global correction is applied to the hypothesized shape provided in the previous step. This is the key step of the process and the one which is the great innovation in the sense of including statistical information about shape. This part will be preserved.

Lets focus on the prediction step. Notice that if we apply just this step to segment any structure without the regularization process, we will get a poor segmentation method that is not able to deal with most of the structures appearing medical imaging. Thus, we realize that what makes ASM a really powerful method is its regularization step. So any intent to improve ASM, passes through the improvement of its prediction step. This is exactly what we will do in this work.

Our main aim is to give a general framework for medical imaging segmentation which will be composed of the two previously mentioned steps. By general framework, we do not mean a unique segmentation method that is exactly the same for every structure and every imaging modality. This would contradict what we mentioned in section (5.6). But, given any segmentation problem, image properties have to be taken into account so that an appropriate prediction step can be derived, meanwhile regularization step does always remain the same.

This framework allows the fully integration of a priori knowledge of shape to any segmentation method (snakes, balloons, optical flow etc.) to enhance its performance. Deformable models and particulary ACM, are powerful segmentation methods that exploit visual cues to derive external forces that drive the snake to the desired boundary. Nevertheless they are local methods in the sense that each node evolves according to its neighbors and some criterions about elasticity and smoothness but without taking into account the global shape of the target structure. Thus, mixing them with a priori knowledge given by PDM in a common framework, will lead to a robust segmentation method that includes both, low and high level information. We call it Generalized Active Shape Models (GASM).

7 GASM Applied to Contrast Echocardiography Segmentation

7.1 Introduction

Most of the work for analyzing automatically the myocardial perfusion, have been done using SPECT or MR imaging: [48], [49], [51], [50]. Due to the novelty of contrast ecocardiography imaging less work have been developed, however some approaches have been done in the framework of tracking myocardial points but they are reduced to some ROIs. These have to be actualized due to the myocardium motion in order to extract meaningful data. The easiest way to do so is by manually actualize them. Nevertheless, the great amount of images and the lack of identifiable landmarks inside the myocardium, emphasizes the need for automatic methods. First attempts ([45], [46]), have been done in the field of optical flow [80]. Also non-rigid registration have been proposed in works such [81]. In [47], it is proposed to segment the ventricle walls by using ACM and ASM. This fits our proposed two-step framework for image segmentation nevertheless, the authors model the shape with the first M coefficients of its discrete cosine transform instead of the raw coordinates which is not considered for us though it is an interesting approach. Our method [53] has similarities to them. We segment the full myocardium in order to track the whole contour. To achieve it we apply GASM combining ACM and ASM, which allows us to take advantage of the experts knowledge (a priori knowledge) about variability of the target structure.

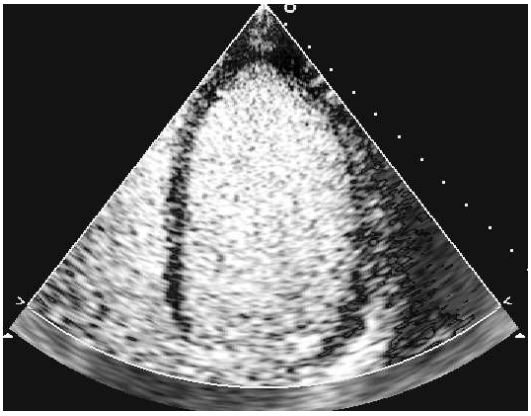

Figure 13: Frame of contrast Echocardiography. The inverted U-shape is the structure to be segmented, the myocardium seen in the long axis view.

7.2 Analyzing Image Drawbacks

Despite contrast agents have lead to imaging quality enhancement, the difficulty for contour definition in echocardiography still remains. Thus, the target structure (Figure 13) may not be easy to segment due to the lack of some of its parts. We first analyze all the drawbacks that our images may present. Figure 14 shows an instance of each of them.

- In Figure 14.a, we can appreciate the lack of right side border of the *myocardium* and in Figure 14.b, both of them are missing. In this frame we also can appreciate a gap inside the right branch. This is the *papillary muscle*, a structure of the myocardium that has to be ignored by the segmentation because it does not provide relevant information.
- In Figure 14.c, we can appreciate at the top of the image a gap along the *endocardial* border. This is not any myocardial structure, but it is an image artifact.
- In Figure 14.d, corners of the *myocardium* are vanished.
- In Figure 14.e, we can appreciate the low contrast presented between the *myocardium* and the background. The left *myocardium* branch has almost disappeared.
- In Figure 14.f, we can appreciate how the right branch of the *myocardium* is stacked on the left border of the visual field.

Now that we have the problem in mind it is time to develop a strategy that allows us to segment the myocardium properly. Our purpose is to apply the framework that we have proposed in the previous section: GASM. This will consist of two main steps: Prediction and Regularization.

7.3 Prediction Step Background

The best way to develop this step is just to think of the best segmentation method we would apply to the problem without considering the regularization step. This last will always improve the prediction so, the more accurate the first step is, better results we will get.

As prediction step we will use ACM techniques, nevertheless our snake will differ from classical snakes in the synthesis of its external forces (F). We will derive these forces from simple image characteristics namely, contours extracted by an ordinary edge detector and gradient directions. This way, our snake

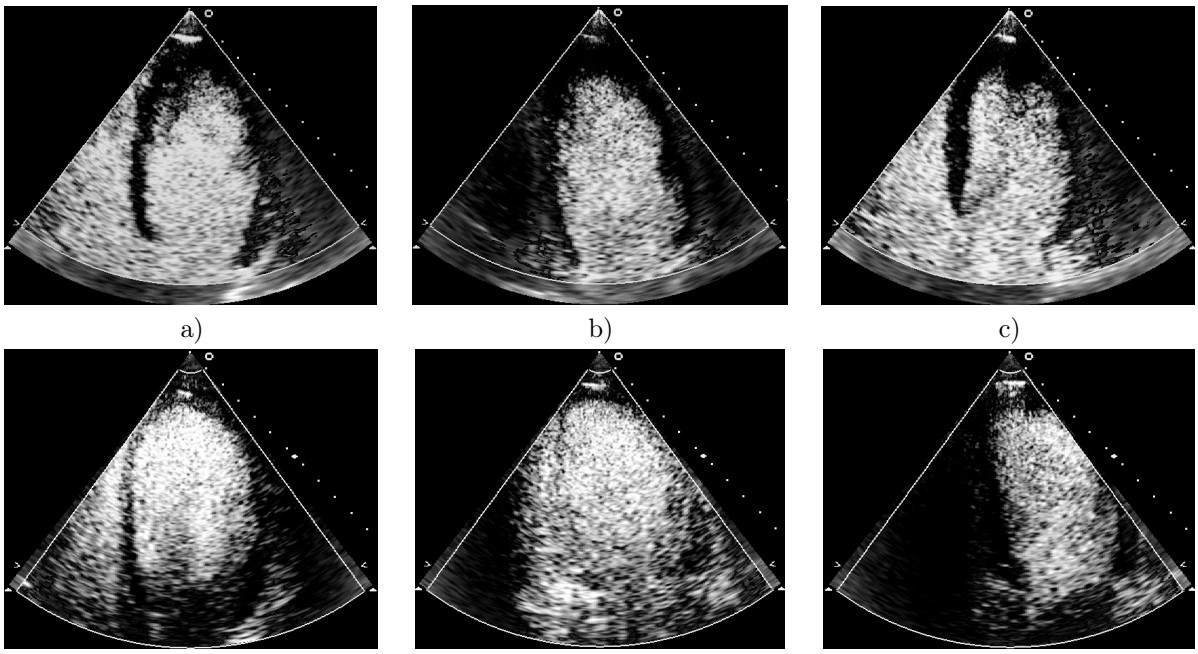

Figure 14: Different artifacts that can be found in Contrast Ecocardiography. Among them, lack of borders, vanishing of structures, gaps, etc.

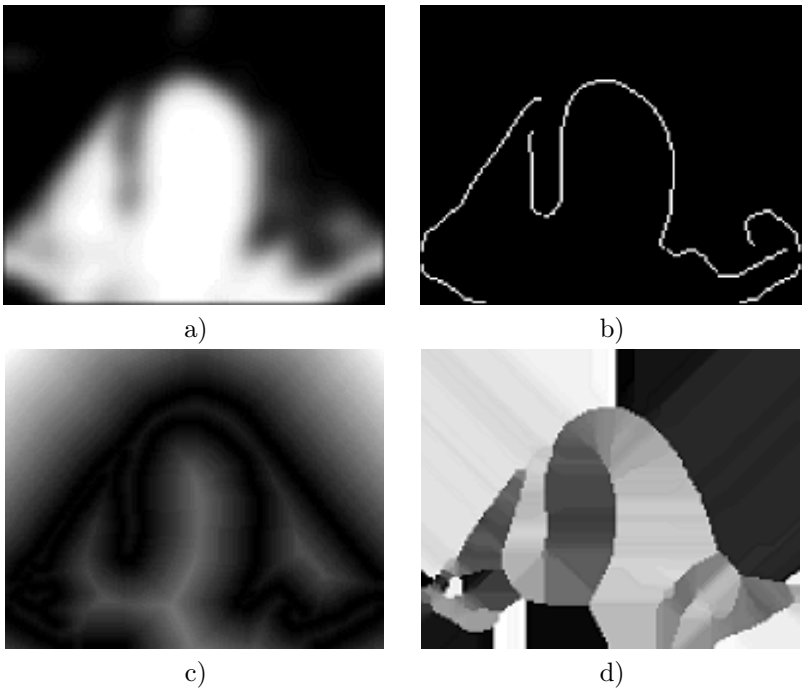

Figure 15: Filtered image a). Edges extracted by Canny b). Distance Map c). Angle Map d).

will not be attracted by any nearby contour, but only those that meet certain properties that we will impose.

In order to get good results, a preprocessing of the images must be done to smooth the speckle appearance (typical in ultrasound images) while preserving as much as possible the image contours. For this reason, given an image I, it is filtered using an anisotropic diffusion filter [52], thus obtaining I_f. Figure 15.a shows its performance. Now, using an edge detector, Canny for instance, contours from the filtered image are extracted (I_c) (Figure 15.b). One of the two ingredients that will compose our external force will be extracted from the gradient direction of I_f over the contours in I_c. The second will be the normal vectors of the snake ant each node. Mixing them we will impose that the condition by which a snake node is allowed to be attracted by a contour is that the normal vector of that node is similar than the gradient direction of the nearest contour. By similar, we will understand that their angle absolute difference between these vectors is less than $\pi/2$.

The numerical implementation of equation (6) from section (5.2) allow us to deform the snake (thought in practice as a set of nodes) until it reaches the global minimum which is supposed to coincide with the image boundaries. It is as follows:

$$\begin{cases} x_{t+1} = (A + \gamma Id)^{-1}(\gamma x_t + F_x(x_t, y_t)) \\ y_{t+1} = (A + \gamma Id)^{-1}(\gamma y_t + F_y(x_t, y_t)) \end{cases} \tag{26}$$

where A (the scatter matrix) codifies the smoothness constraints, γ affects to the speed convergence and $F = (F_x, F_y)$ are the external forces that make the nodes move. F is often directly defined as $F = - \bigtriangledown P(x, y)$, where P is usually any of (5) or (4). Nevertheless, to fit our purposes, we will synthesize the following external force:

$$F(x, y) = -\langle \overrightarrow{v_c}(x, y), \overrightarrow{v_s}(x, y) \rangle \nabla D(x, y) \tag{27}$$

where D is the distance map (Figure 15.c) obtained by propagating distances from the contours in I_c, $\overrightarrow{v_c}(x, y)$ is the gradient direction of I_f in the nearest edge point to (x, y) (in distance D) and $\overrightarrow{v_s}(x, y)$ is the normal vector to the snake, fixed one of the two possible, at the point (x, y). Three issues have to be mentioned:

- First of all, notice that $\overrightarrow{v_s}(x, y)$ is not defined $\forall (x, y) \in \mathbb{R}^2$, but only in the snake node that, at this moment, is placed over (x, y).
- The same way we previously have created the distance map D (by propagation), we have to create an angle map D^{Ψ} (Figure 15.d) so that, at each point (x, y) we know not only the distance to the nearest edge point but also the gradient direction of it [5]. This is also done by information propagation.
- Let

$$\underbrace{\langle \overrightarrow{v_c}, \overrightarrow{v_s} \rangle}_{K} = \begin{cases} (0,1] & \text{if} \quad \text{angle}(\overrightarrow{v_c}, \overrightarrow{v_s}) < \pi/2 \\ 0 & \text{if} \quad \text{angle}(\overrightarrow{v_c}, \overrightarrow{v_s}) = 0 \\ [-1,0) & \text{if} \quad \text{angle}(\overrightarrow{v_c}, \overrightarrow{v_s}) > \pi/2 \end{cases}$$

The term K makes the snake be attracted by contours that have similar orientation (angle between $\overrightarrow{v_c}$ and $\overrightarrow{v_s} < \pi/2$) and rejects it from contours which have opposite directions (angle $> \pi/2$). In

case that $K = 0$, the only forces that act in these points are internal forces. Figure 16 depicts this idea.

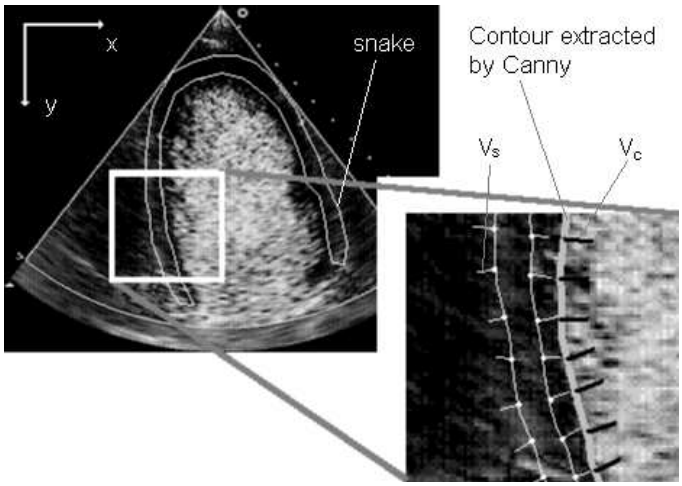

Figure 16: A detail of the constraints that the external force apply to the snake.

7.4 Regularization Step Background

To apply the regularization step to the process and thus incorporate a priori knowledge about shape, first of all the PDM has to be created. To this end, a training set made of 70 images from four different cardiac cycles had been created. This set covered the wide range of shape variation. An expert clinician was asked to manually label 40 landmarks on every image to delimitate the myocardium structure. After the PCA was applied, a PDM was obtained with 10 principal modes of variation which could explain the 98.5% of the shapes in the training set. In Figure 17 we can appreciate the first eight modes of variation.

7.5 Initialization

As we have told, the initialization of the model is a problem that has to be separately treated as there is not a unique way to do it. What it is certainly common is that the model has to be placed near the final result. Initialization can be as sophisticated as desired depending on if our aim is to reach a fully automated method or a semi-automated method. In the present work, we developed an initialization method that fully automatize the segmentation process.

We have selected four key points over the shape model. These, as shown in Figure 18.a, are the left and the right corners (C_L and C_R) and the top points of the *endocardium* and the *epicardium*, the internal and external part of the *myocardium* respectively (T_I and T_E). Thus, to initialize our snake (S_0), we will search for these points on the image and wrap the mean shape so that its key points fit those in the image, $\bar{X} \longmapsto S_0$ (Figure 18.c).

To find the corners we use the Harris Corner Detector. Once found, we look for the most significant gradient of $I(x, y)$ along the line defined by points $C = (C_L + C_R)/2$ and T, where T is the top point of the sectorial ROI that contains the echocardiogram, this gives us T_I . As we could observe in most of the frames, the point T_E remains almost fixed, so we consider it fix (Figure 18 (b)).

Notice that the implementation of the corner detector allows the fully automatization of the process nevertheless, a minimal-human-initialization would consist of just marking manually these two points.

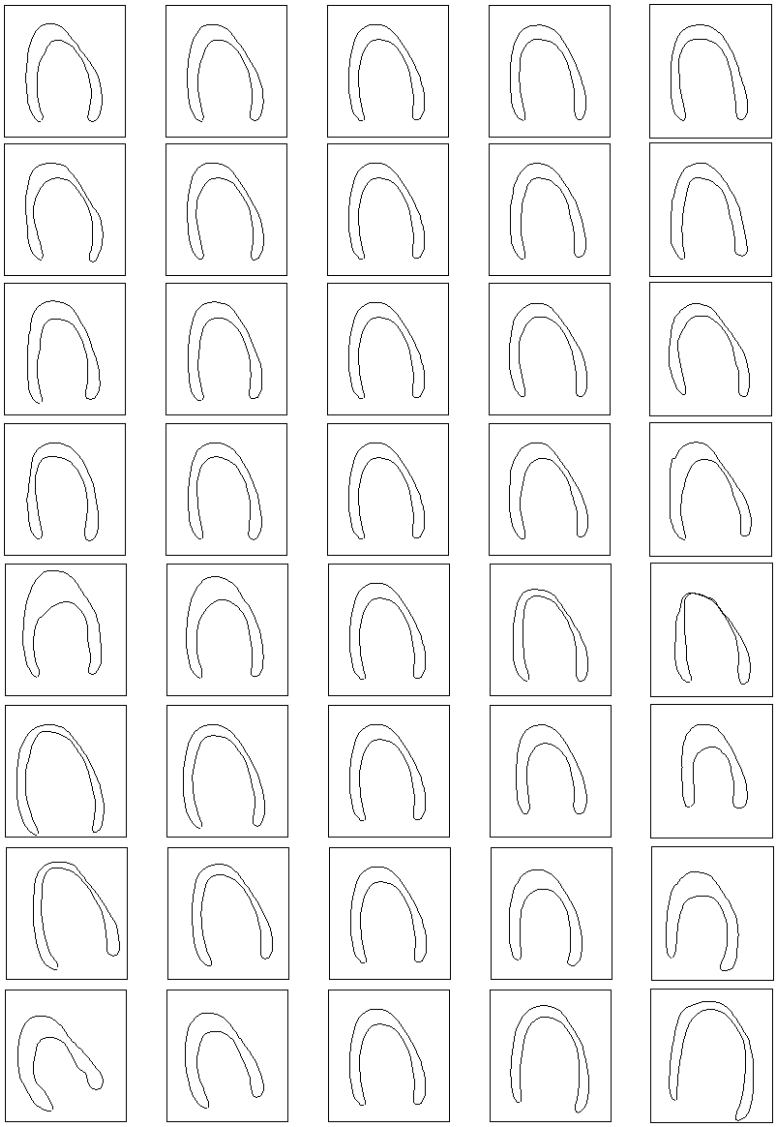

Figure 17: First eight modes of variation. Each row represents one of them and is specialized on a particular aspect of the shape. Central column is common for all variation modes due it is the mean shape.

7.6 GASM Performance

Now that we have developed a prediction method (the snake guided by special forces) and we have trained a PDM (regularization step), it is time to apply our segmentation framework: GASM.

Given the snake at time t, $S_t = \{(x_{s,t}, y_{s,t})_{s=1}^{M}\}$ we hypothesize the new position of the snake nodes $\widetilde{S}_{t+1}$ by applying eq. (26). We regularize $\widetilde{S}_{t+1}$ looking for the most similar valid image given by our PDM. First of all, we have to align $\widetilde{S}_{t+1}$ (we apply the similarity $M_{\theta,r,T}$) and then project it into the shape space to get the parameters b as in Eq. (22). Then we get the plausible shape by Eq. (21) and finally, to get the next snake S_{t+1}, we disalign X (undo the similarity: $M_{T,r,\theta}^{-1}$). This can be condensed by the following equations:

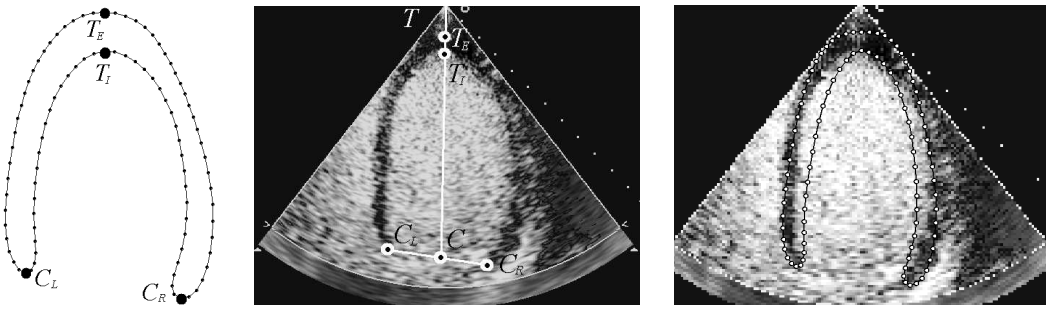

a) b) c)

Figure 18: Mean shape $\overline{X}$ a). Key points found in the target frame b). Initial Snake: mean shape warped to fit the key points c).

$$\begin{cases} \widetilde{S}_{t+1} = (A + \gamma Id)^{-1}(\gamma S_t + F) \\ S_{t+1} = M^{-1}_{T,r,\theta}[\overline{X} + PP^T(M_{\theta,r,T}(\widetilde{S}_{t+1}) - \overline{X})] \end{cases} \tag{28}$$

If we iterate the process, once evolving followed by correcting, we realize that the shape constraints given by the PDM are too strong and hardly lets the snake search for new positions (as we mentioned in the previous section). To solve this we apply the corrections every Q steps. In this particular problem we used $Q = 2$.

In Figure 19 we show the evolution of the initial Snake under the GASM framework.

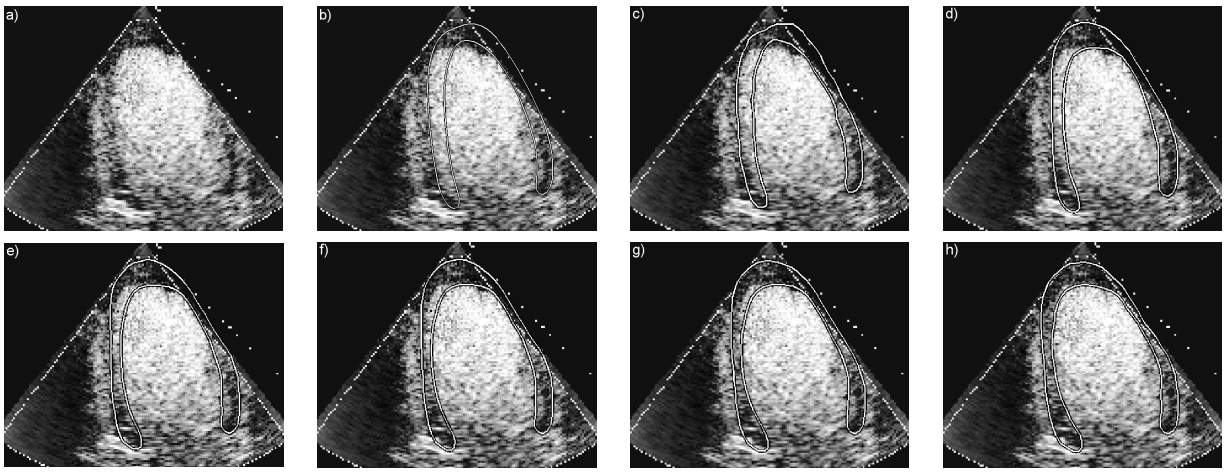

Figure 19: Segmentation process: Target frame a). Initial Snake b). Snake at time steps $t = 1, 2, 5, 7, 10$ c), d), e), f) and g). Convergence at $t = 17$ h).

7.7 Discussion

We would like to mention the advantages given by the GASM segmentation framework and how it deals with the drawbacks of images introduced in section (7.2):

- The natural smoothness constraint that ACM have implicitly, avoid that the snake falls into the spurious gaps (Figure 14 (c)) or heart structure gaps (Figure 14 (b)) that may appear in the images.

- The special external forces that we have tailored for this problem in particular, avoid the *epicardium* contours shrink to *endocardium* contours when they are not present as in (Figure 14 (a) and (b)). This is due to the fact that their gradient direction is opposite (not similar).

- PDM apart from regularizing the hypothesized shape, deals with drawbacks that the snake cannot. For instance when contour information is not available at all, as in Figure 14 (e) or when the branch has collapsed as in Figure 14 (f). Notice that this last case is particularly modelled by the 5^{th} variation mode (Figure 17).

8 GASM Applied to Tagged MRI

8.1 Introduction

In this section, we will introduce a novel method that allows us to track myocardial points along the cardiac cycle called HARP (harmonic phase) tracking, and which will be used as the prediction step in our GASM segmentation framework. We will derive a method that allows both, point tracking and *myocardium* segmentation.

From point tracking and structure segmentation many information will be derived such myocardial stress and strain, rotation etc. By expanding point tracking to 3D, the reconstruction and movement of the myocardial fibers will become available allowing for the prove or disprove of the *ventricular band* existence.

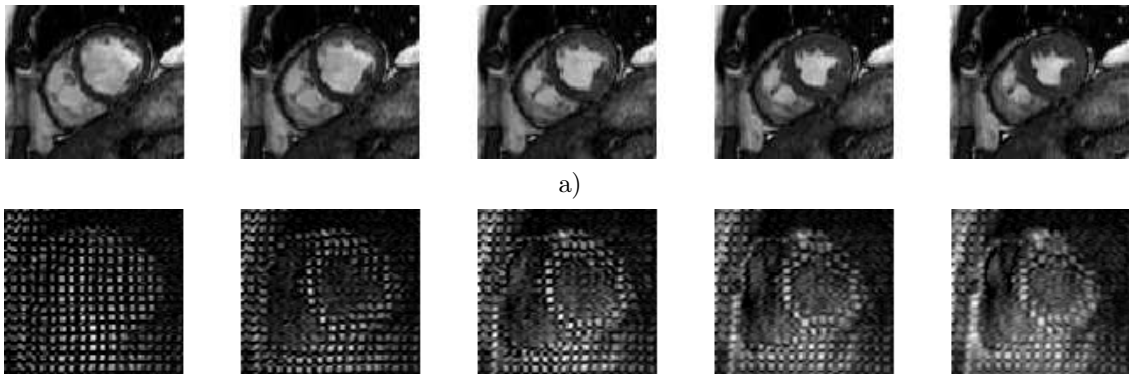

a)

b)

Figure 20: a) Ordinary MR sequence. No landmarks are appreciated over the myocardium. Only Contraction activity can be appreciated. b) TMR sequence. The tissue tagging reveals myocardium points movement.

8.2 SPAMM Tagging

SPAMM is the acronym for SPAtial Modulation of Magnetization, thus what SPAMM tagging does is precisely this. Given a tomographic magnetized plane in MR images, this method applies a special radio frequency (RF) pulse that modularizes the underlying magnetization of the tissue making appear dark stripes or tags (Figure 20 (b)). Due to the fact that these tags are a property of the hydrogen atoms of

the *myocardium*, they will remain the same as the heart beats and the tags will move according to the underlying movement of the myocardium.

The simplest tagging pattern is the 1D 1-1 SPAMM that applies one single RF pulse. Let every material point be marked by its position $p \in \mathbb{R}^3$ at the reference time $t = 0$, which is usually considered at *end-diastole* when the left ventricle is full of blood and the heart is relatively slow-moving. Let $I(p)$ be the intensity of this material point in absence of the tag pulse sequence. This is the magnetization provided by ordinary MR. The application of an 1D 1-1 SPAMM tag pattern [55]

$$s^1(p; w, \alpha) = \cos^2(\alpha) + \sin^2(\alpha)\cos(w^T p) = d_0(\alpha) + d_1(\alpha)\cos(w^T p) \tag{29}$$

will produce the image

$$I_1(p) = I(p)s^1(p; w, \alpha) \tag{30}$$

where α is the so called tip angle and w is the gradient that determines the direction and the width of the tags. To produce a bidimensional tag pattern, 2D 1-1 SPAMM, two 1D 1-1 SPAMM sequences are applied in rapid successions with linearly independent gradient directions w_1 and w_2 and tip angles α_1 and α_2, which produces

$$I_2(p) = I(p)s^1(p; w_1, \alpha_1)s^1(p; w_2, \alpha_2) \tag{31}$$

Substituting (29) in (31) and using the following trigonometrical identity

$$\cos(\alpha)\cos(\beta) = \frac{\cos(\alpha + \beta) + \cos(\alpha - \beta)}{2} \tag{32}$$

the 2D tagged image I_2 can be written as the sum of four other images that are tagged using 1D patterns

$$I_2(p) = \sum_{i=0}^{4} I(p)d_i(\alpha_1, \alpha_2)\cos(w_i^T p) = \sum_{i=0}^{4} D_i(p; \alpha_1, \alpha_2)\cos(w_i^T p) \tag{33}$$

where the functions d_i, $i \in \{0, \ldots, 4\}$ are easy to deduce and $w_0 = 0$, $w_3 = w_1 + w_2$ and $w_4 = w_1 - w_2$. An improved version of 2D 1-1 SPAMM is proposed in [56] and it considers more RF pulses with their relative amplitudes distributed according to the binomial sequence, resulting in sharper stripes. This finest tag pattern is given by

$$s^{N-1}(p; w, \alpha, \theta) = \sum_{k=0}^{N-1} d_k(\alpha)\cos(kw^T p) \tag{34}$$

The resultant tagged image can be written as

$$I_2(p) = \sum_{k=0}^{K} D_k(p; \alpha_1, \alpha_2)\cos(w_k^T p) \tag{35}$$

where $K = (N-1)^2$.

8.3 SPAMM Tagged MRI Analysis Techniques

Given a volume of tagged images, it is certainly difficult to extract conclusions. First techniques of computer-assisted analysis of SPAMM tagged MRI were proposed by the same creators of this tagging technique. In [58] they perform manual marking of tag intersections and follow them along the sequence. In [59] spectral filters are used in order to isolate frequential components produced by SAPMM tagging so that filtered images are prepared for their tags to be detected. In [60], in addition, a modification of

the histogram is performed to enhance image contrast between tags and tissue. Some other works use ACM to localize and track the tags in time. In [61], they use the so called implicit snakes, 3D B-splines, in addition to two coupled surfaces that deform to fit myocardium borders. In [63] 4D B-splines are used. In [62] morphological techniques are used to eliminate tags in order to segment myocardium while tags are tracked by matching a template of their expected profile using least squares. [69] use truncated polynomial expansion and [70] use a stochastic estimation scheme.

All these analysis techniques are developed to track tag lines and even supposing that their performance is optimal, there is problem left. This is that they are able to track only points over the tags but not points between them. The application of some interpolation process is required in order to get dense motion estimation.

HARP (HARmonic Phase) is a novel and fast technique that overcomes the previous drawback. It is a spectral method that naturally provides information about the movement not only of tag points but also inter-tag points. This method was introduced by Osman *et al.* ([64], [65], [66]). Some works as [68], use HARP principles and orthogonal myocardium views (short axis and long axis) in combination to a 3D geometric model based on finite elements to estimate the real movement. A similar approach is exposed in [67].

8.4 HARP: Frequency Domain Analysis

The key point in tagged MR image is not to study them in the spatial domain but in the frequency domain, where the spectral peaks (Figure 21.a) contain information about motion, each of them in a certain direction. If we filter a single peak, back in the spatial domain we get a complex image the phase of which is linearly related to the directional component of the true motion. Obtaining the phase is quite difficult due to the tangent operator, even though we will see that the principal values of the phase, lying in $[-\pi, \pi]$, are enough to estimate small motions.

Notice that equation (35) can be rewritten as

$$I_2(p) = D_0 + \sum_{k=1}^{K} D_k \frac{e^{i(w_k^T p)} + e^{-i(w_k^T p)}}{2} \tag{36}$$

what makes appear $(2N-1)^2$ spectral peaks in the Fourier domain (Figure 21). This gives us the opportunity to isolate any of the summands of the expression (36) by filtering its correspondent peak.

Expression (36) is a formulation valid just for the first frame, the reference frame. As the heart deforms, a material point within the *myocardium* moves from its reference position p to a new spatial position x at time t and it is given by the reference map $p(x;t)$ so, for any point x in any frame (time t), we have the formulation

$$I_2(x;t) = D_0 + \sum_{k=1}^{K} D_k \frac{e^{i(w_k^T p(x;t))} + e^{-i(w_k^T p(x;t))}}{2} \tag{37}$$

Notice that filtering the *nth* spectral peak, we obtain the complex function

$$I_n(x;t) = \frac{D_n}{2} e^{i(w_n^T p(x;t))} \tag{38}$$

in which its phase is linearly related to the reference map

$$w_n^T p(x;t) \tag{39}$$

This means that the phase is an intrinsic property of the material points, thus if we are able to track their phase, we will also be able to track them. Nevertheless, we will not be able to calculate the phase due to the arc tang operator wrapping effect. Instead we will calculate its principal values which will

provide the so called HARP images (Figure 21 (b), (c)). These will be crucial in motion tracking. The HARP image associated to a given spectral peak is defined as

$$a_n(x;t) = \angle I_n(x;t) = \begin{cases} \tan^{-1}(\frac{Im(I_n)}{Re(I_n)}) & Re(I_k) \geq 0 \\ \tan^{-1}(\frac{Im(I_n)}{Re(I_n)}) + \pi & \text{otherwiswe} \end{cases} \tag{40}$$

It is worth to mention that despite the true motion of the heart is in 3D, in this work we consider just the apparent motion that is in 2D. This means that we assume that the gradient directions of the tagging pulse are parallel to the image plane thus, what we see in the images are projections of the real movement.

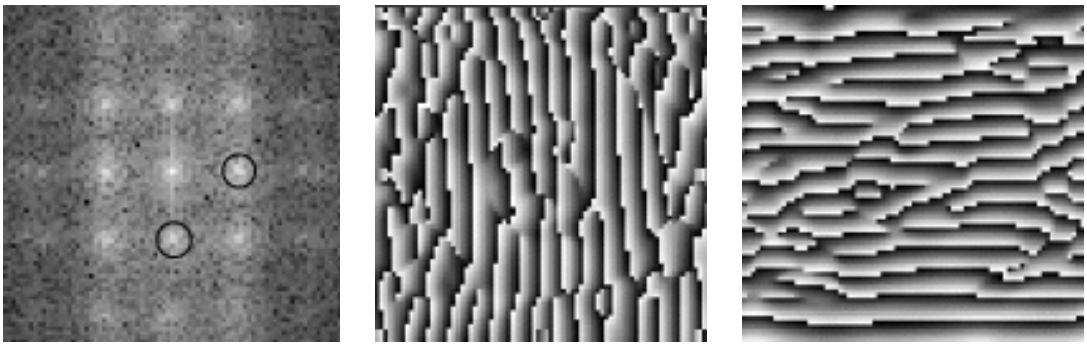

a) b) c)

Figure 21: TMR Fourier transform with the main harmonic peaks in orthogonal directions to be filtered a). HARP images obtained by filtering two of the principal harmonics in orthogonal direction, vertical b) and horizontal c).

8.5 Motion Tracking Using HARP Images

In this section we present the engine that makes possible the point tracking and which is based on the previously introduced HARP images.

Given any frame in a tagged sequence, I^i, we can calculate its HARP images, $\phi_h(x;i)$ and $\phi_v(x;i)$, (Figure 21 (b), (c)) which embed tag information in both directions, horizontal and vertical, by filtering the principal spectral peaks in these direction (Figure 21.a). Thus given any point $x \in I^i$ we can associate to it a pair of angles. Those that share the same coordinates in ϕ_h and ϕ_v, $x \longmapsto \phi(x;i) = [\phi_h(x;i), \phi_v(x;i)]^T$.

Recall that phase is an intrinsic property of the tissue, thus the key is to realize that any point will maintain its pair of angles along the whole sequence. To calculate the position of a given point $\tilde{x}$ in the next frame , x, we look for the nearest point (in the next frame) that possesses the same pair of angles. This condition is written as

$$\phi(\tilde{x};i) = \phi(x;i+1) \tag{41}$$

and finding $\tilde{x}$ is equivalent to solve the following bidimensional non-linear equation

$$\phi(\tilde{x};i) - \phi(x;i+1) = 0 \tag{42}$$

which is done by applying the Newton-Raphson iteration method

$$x^{n+1} = x^n - [\nabla\phi(x^n, i+1)]^{-1}[\phi(x^n, i+1) - \phi(\tilde{x}, i)] \tag{43}$$

Details about the practical implementation of equation (43) are exposed in [71].

8.6 GASM applied to Tagged MRI

HARP method is a powerful technique that provides optical flow in SPAMM tagged sequences and it is particulary well suited in obtaining such information for all points so no interpolation process is required. Nevertheless we want to know the displacement map not for all of them but only those in the *myocardium*. Due to the fact that HARP method does not incorporate structural information, we will embed a segmentation process in it. This will allow to avoid calculations in the outer points and process will become faster. Apart, obtaining *myocardium* segmentation which is of importance in itself. We will mix both, point tracking and segmentation in our proposed segmentation framework: GASM.

8.6.1 Prediction Step Background

Recall section (7), to segment *myocardium*, the inverted U-shape, we applied GASM scheme where the prediction step used an ACM. In the current problem it seems complicated to synthesize external forces that can drive a snake through all the tag ridges without getting stacked on them. Nevertheless in our segmentation scheme (GASM), prediction step not always has to be an ACM. The philosophy is that this step has to be tailored for the current image characteristics. This is precisely what we have done. We use the displacement map provided by HARP method as the prediction step.

We define the displacement map as

$$\begin{cases} u : \mathbb{U} \times \mathbb{R} \longrightarrow \mathbb{U} \\ \quad (x; i) \longmapsto \hat{x} - x \end{cases}$$

where $\mathbb{U}$ is the image domain and $\hat{x}$ is the solution of the equation (42). This map tells us given a point x in the ith frame, where it is going to be in the $(i+1)th$ frame.

Thus given the *myocardium* contour in the ith frame, which is thought as a set of M nodes as any snake, $C^i = \{x_k^i\}_{k=0}^M$, we predict its next position in the $(i+1)th$ frame by

$$\tilde{C}^{i+1} = \{\tilde{x}_k^{i+1}\}_{k=0}^M \tag{44}$$

where $\tilde{x}_k^i = u(x_k^i, i)$.

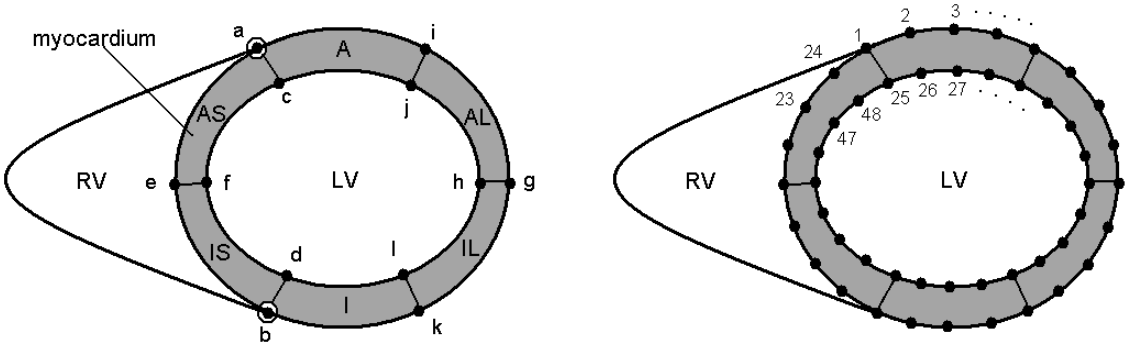

a) b)

Figure 22: a) The 12 key points that divide the myocardium in 6 parts: A, AS, AL, I, IS and IL and which are used to mark the rest of points. b) Labelling order of the 48 points that are used to represent the myocardium shape.

8.6.2 Regularization Step Background

Due to the fact that tags outside the *myocardium* are not stable because of the blood flow, among others, HARP performance in the borders is not as precise as inside. This can often lead to a bad prediction of the segmentation proposed by equation (44) in the previous step. For this reason, the regularization step is required.

As ever, we will model *myocardium* shape variation in a PDM. To label points in the structure borders, we will consider 12 key points that will serve as reference for a further ordered labelling. These are the meeting points of the RV and LV *epicardium*, a and b, with their projections to the *endocardium*, c and d; middle point between a and b, e (with its projection f); the same to the other side produce g and h and finally the same between a and g, and b and g is performed in order to obtain i, j, k and l (Figure 22 (a)). These points divide the *myocardium* in four different regions namely, *anterior* (A), *anterior septum* (AS), *anterior lateral* (AL), *inferior* (I), *inferior septum* (IF) and *inferior lateral* (IL). These parts will be useful when extracting information from point displacement. Having marked the key points, we in addition mark three equally-spaced points among them which turns to a shape represented made of 48 points. Their labelling has to be done always the same way. We do it as shown in Figure 22 (b).

To derive the PDM we collected 165 images to create the training set that covered the range of shape variation appreciated in the myocardium. These were not tagged MR images because point labelling is more difficult in them due to the tagged appearance. Despite of that we used ordinary MR images where the structure of the myocardium is the same and, in addition, LV is well contrasted. Thus the labelling becomes friendlier. After applying the PCA to the extracted shapes, we obtained a 10-dimensional model that could explain 97.75% of the shape variation appreciated in the training set. Figure 23 show the first seven modes of variation.

8.7 Initialization

It is difficult to fully automatize the segmentation process, for this reason we manually perform the first segmentation (minimal human-interaction). Nevertheless, such initialization can not be performed to the first frame due to the fact that this frame is completely tagged, even blood, making almost impossible to distinguish the target structure (Figure 24 (a)). Instead of this, we will initialize the segmentation in the second frame C^2 and calculate the segmentation of the first frame by applying the inverse of the first displacement map u_1^{-1} as

$$\tilde{C}^1 = \{\tilde{x}_k^1\}_{k=0}^M \tag{45}$$

where $\tilde{x}_k^1 = u^{-1}(x_k^2, 2)$

It is possible that even the second frame it is difficult to segment. The idea is also applicable in this case. We segment the third and we calculate the previous segmentation using first and second inverse displacement maps. In fact this can be generalized so that it is plausible to start with any frame.

8.8 GASM Performance

Once both, the prediction step is created and PDM derived from the training set, we apply the GASM framework. Notice that the method that will serve as prediction step will also be used as to obtain dense motion inside the *myocardium*.

We manually initialize segmentation in an appropriate frame, *ith* for instance, then we propagate backwards this initial shape by dilating the ROI given by the manual segmentation. Then we perform HARP method (from previous frame to present) inside this ROI and use the inverse of the displacement map to calculate the predicted previous shape. After this the regularization step is applied in order to obtain a valid shape. This is repeated until first frame is segmented. Then we use forward shape propagation to segment frames from the initial to the last one. HARP method is applied to points

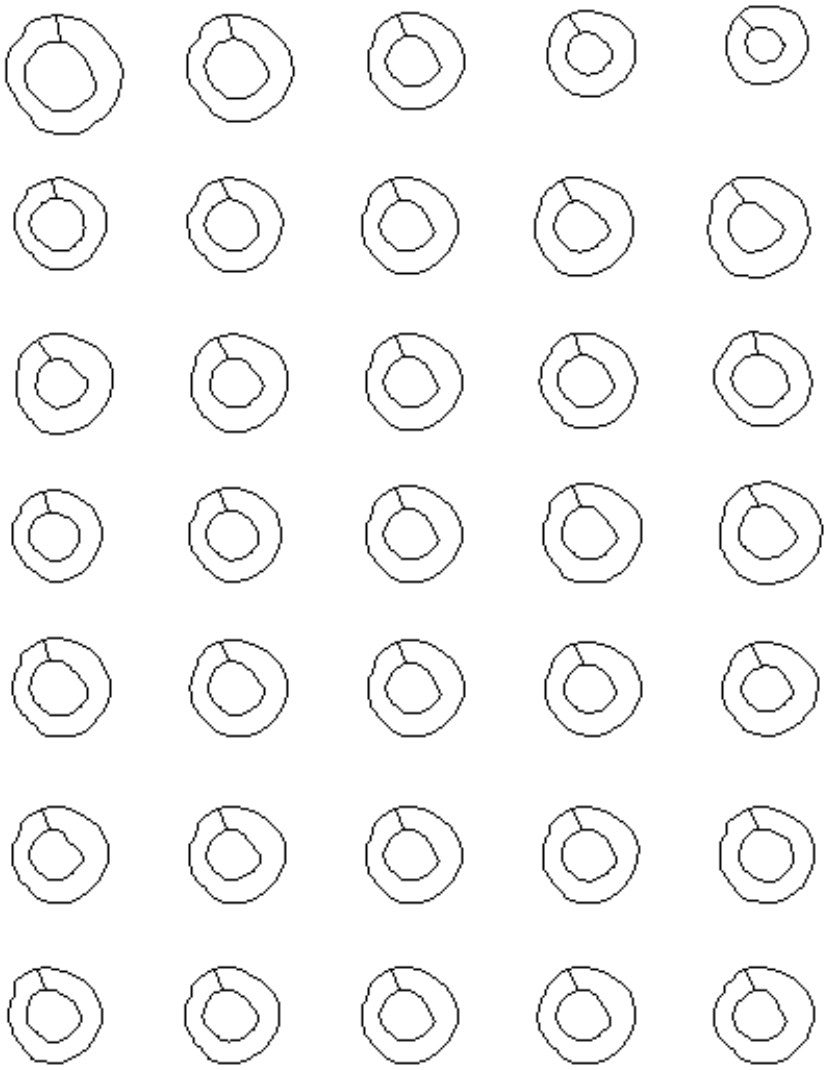

Figure 23: First seven modes of variation. Each row represents one of them and is specialized in a particular aspect of the shape. Central column is common for all variation modes due it is the mean shape.

inside the ROI provided by manual initialization. This time without dilating it. We predict next shape by applying the obtained displacement map and then we regularize it, and so on until last frame is segmented.

The following equations formalize this idea:

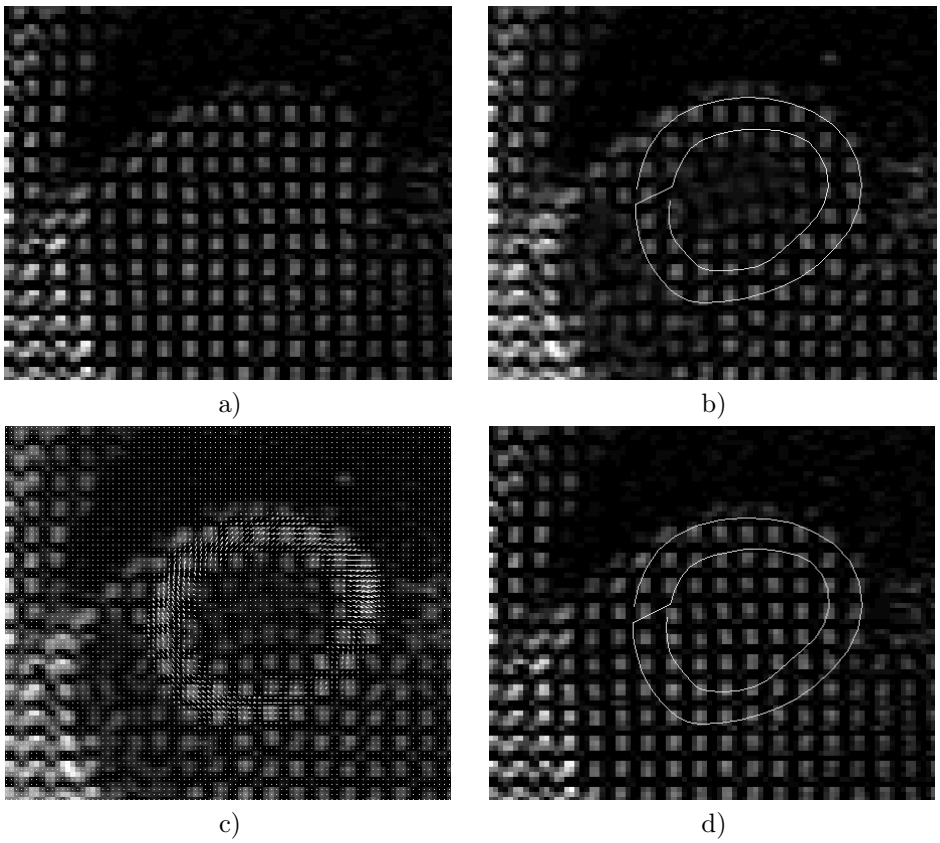

Figure 24: a) Initial frame. Due to the total tagging of the image, it is impossible to distinguish myocardial structure. b) In second frame tagged blood has disappeared so manual segmentation becomes possible. c) Inverse of the displacement map between first and second frame. d) Segmentation of the first frame

$$\begin{cases} C^i & \text{Initial segmentation} \\ \tilde{C}^{j-1} = u^{-1}(C^j, j-1) & \text{Backwards segmentation (prediction)} \\ C^{j-1} = M^{-1}_{T,r,\theta}[\overline{X} + PP^T(M_{\theta,r,T}(\tilde{C}^{j-1}) - \overline{X})] & \text{Backwards segmentation (regularization)} \\ \tilde{C}^{j+1} = u(C^j, j) & \text{Forwards segmentation (prediction)} \\ C^{j+1} = M^{-1}_{T,r,\theta}[\overline{X} + PP^T(M_{\theta,r,T}(\tilde{C}^{j+1}) - \overline{X})] & \text{Forwards segmentation (regularization)} \end{cases} \tag{46}$$

Where $\bar{X}$ is the mean shape of the PDM and $M_{\theta,r,T}$ is the appropriate affine similarity that aligns the current predicted shape to the mean. Recall that in the application of the GASM framework in section (7), we did not applied regularization step every but every $Q = 2$ steps. Here we apply it every step (Q=1).

In Figures 25, 26, 27 and 28, we can appreciate displacement map provided by HARP method, GASM segmentation, tag tracking and synthetic grid deformation respectively.

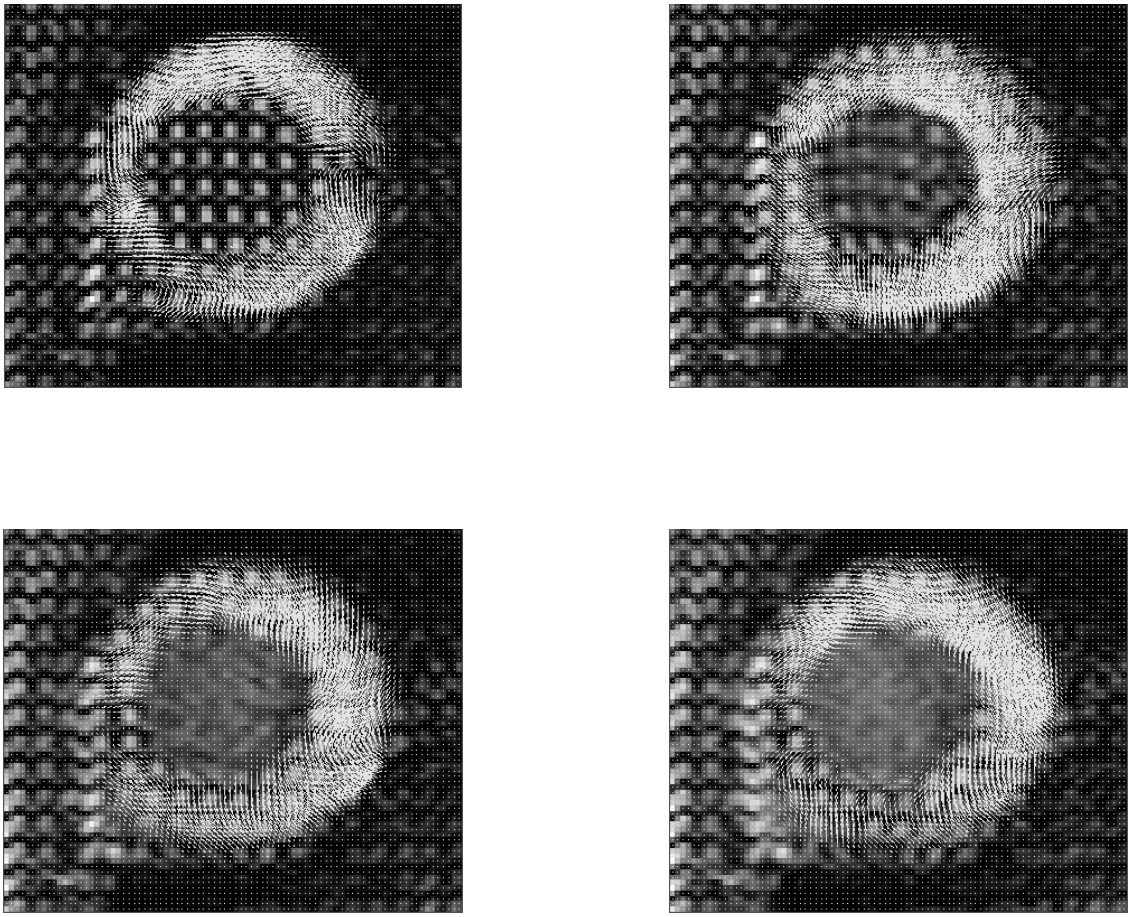

Figure 25: Instance of the displacement map provided by HARP method in a middle SPAMM tagged sequence. The map has been restricted to myocardium due to the influence of GASM segmentation.

8.9 A Simple Clinical Application: Myocardium Rotation.

There are many applications that could be derived from the information extracted by both point tracking and structure segmentation such stress and strain parameters. The concept of strain, a measure of length change or displacement gradient, and stress, the force per unit area on an infinitesimally small plane surface within the material, are of fundamental importance in assessing the regional function of ventricular muscle and measuring myocardial viability in order to classify whether a heart beats normally or not. Other applications can be those that mix information from orthogonal tagged planes (not treated in this work) to construct a full 3D model of myocardial fiber function from which data related to the ventricular band could be obtained. The application we derived from data provided by HARP - GASM, is about myocardial rotation in the six zones in which it is divided namely A, AS, AL, I,IS and IL as depicted in Figure 22 (a). To this end we have calculated the absolute and relative rotation suffered from each point in these particular zones and, as output, we have shown the mean of all of them. This have been done for all frames of a particular tomographic plane.

To calculate the relative rotation suffered from a particular point in the myocardium and in the ith frame, x^i, we consider the angle between the vectors $v^i = x^i - O^i$ and $v^{i+1} = u(x^i, i) - O^{i+1}$, where O^i and O^{i+1} are the centers of mass of the LV in ith and $(i+1)th$ frame respectively; and $u(\cdot, i)$ is the ith displacement map provided by HARP method between frames i and $i+1$ (Figure 29). Absolute rotation

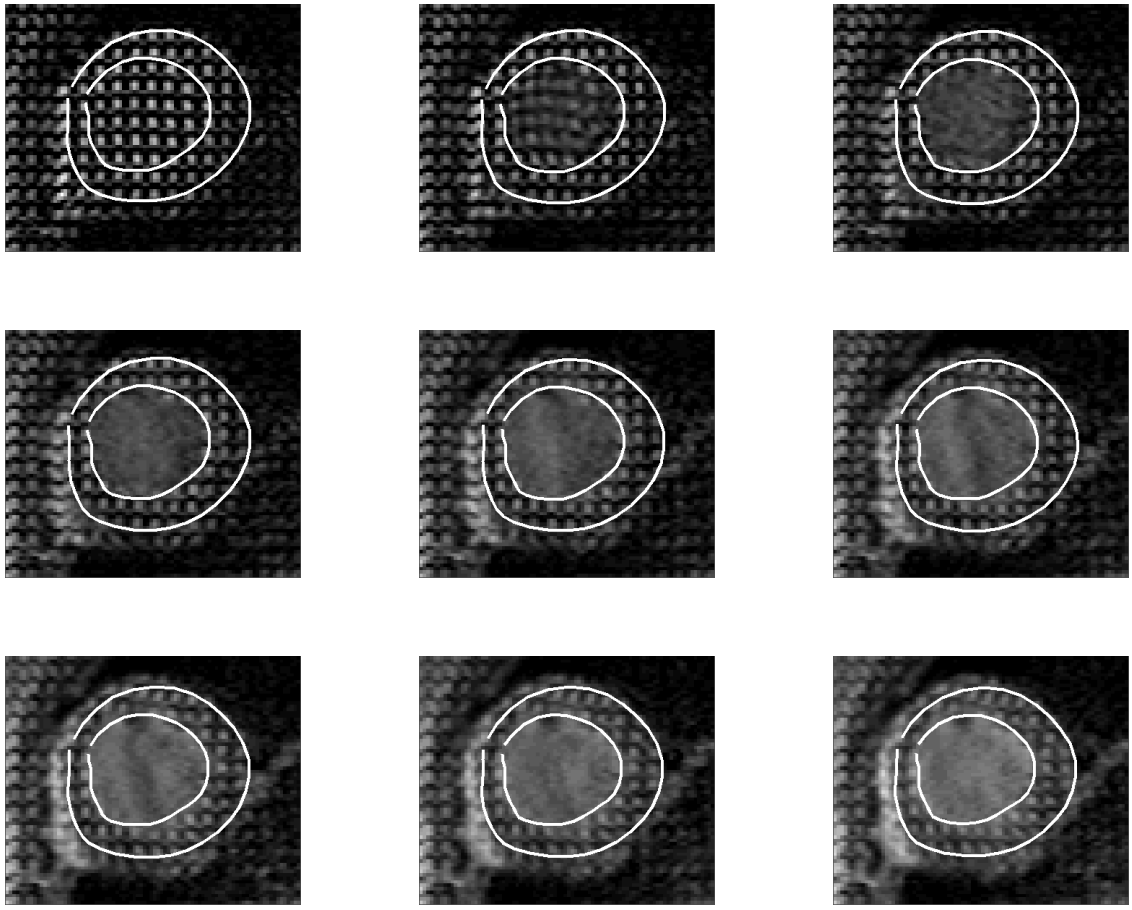

Figure 26: Instance of the segmentation provided by GASM framework in a middle SPAMM tagged sequence.

will be the sum of the previous relative rotations.

Physicians use the rotation information to characterize different pathologies that can affect heart function. Thus, myocardium rotation calculated in the six different zones of the myocardium is a valuable quantitative tool to assess myocardial dysfunctions. In Figures 30 and 31 we show separately rotation information (absolute and relative) in case of healthy adult and a patient with cardiomyopathy, in three acquisition planes belonging to base, middle and apex. In Figures 32, 33 and 34, we depict overlapped rotation information belonging to healthy and pathological (*Myocardiopathy*) patients in basal, mid and apical planes, so that differences appear clearer for the physicians. In the graphics legend, pathology P#1 refers to dilated myocardiopathy, P#2 to myocardiopathy affecting LV contractility and finally P#3 to myocardiopathy affecting RV. Some studies about myocardial rotation (or torsion) are [75], [76] or [77].

8.10 Discussion

In this section we have successfully applied our segmentation framework GASM in which we have embedded the tracking method HARP. Thus, by using HARP we have tailored a prediction step for this particular problem and, by incorporating segmentation information in point tracking, we have avoided multiple useless calculations in outer points.

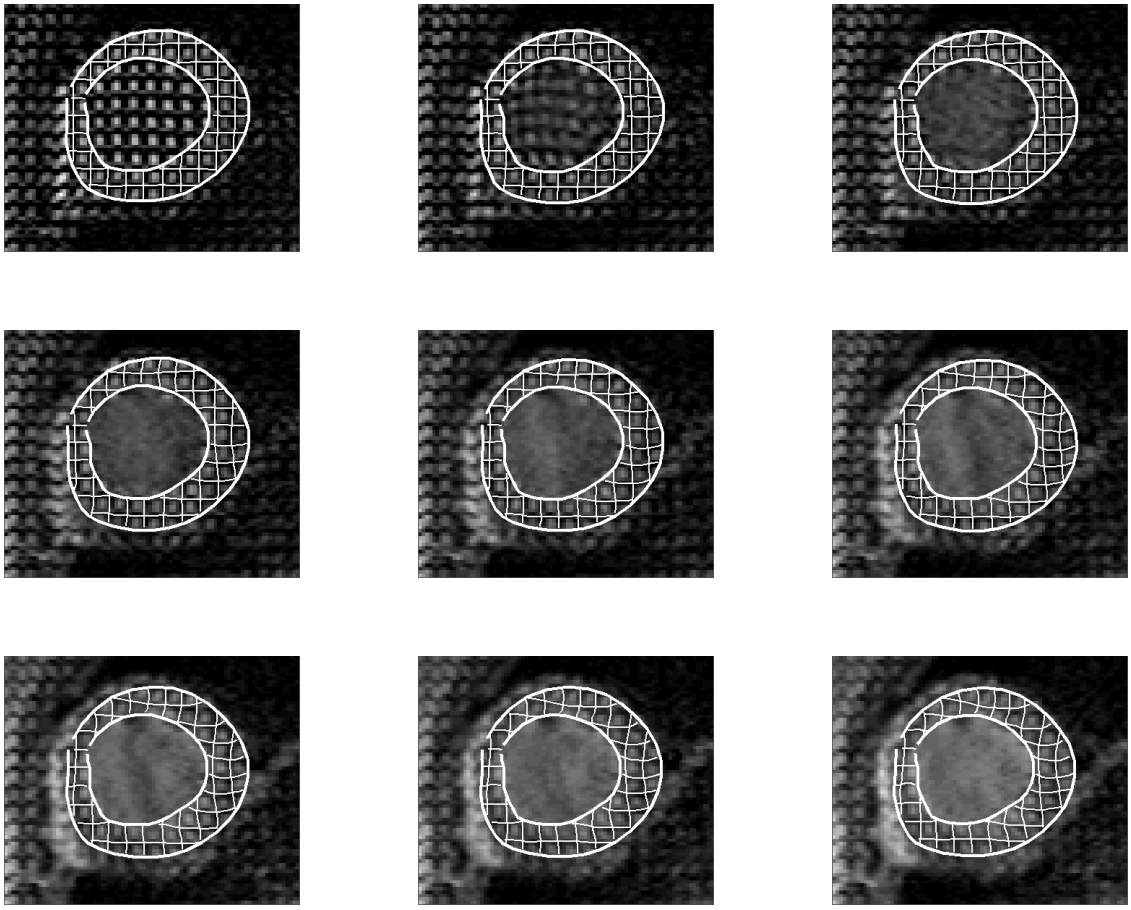

Figure 27: Tag tracking. Tags are manually segment in the first frame and let evolve according to the displacement map provided by HARP method in a middle SPAMM tagged sequence.

We would like to mention a difference between the application of the GASM framework in this problem and in the one exposed in the previous section. In the Contrast Echocardiography, we could segment single frames independently from the others due to the fact that GASM was applied in the snake evolution and the prediction step was the shape proposed by snake forces. This focus differs from the way that GASM has been applied to the present problem. In this one, frames can not be segmented independently because the prediction step is made of optical flow provided by HARP method and it needs the whole sequence to be derived.

9 Results

9.1 On Contrast Echocardiography

Our images were acquired with a Philips Sonos 5500 (Andover, Mass) echocardiography system and the contrast used was Sonovue®. Visualization was performed by the Power- Angio technique. To test our algorithm, we took 180 images of dimension (480 x 385), from 4 cardiac cycles, different from those 50 used to create the training set, and applied (28) to each of them independently. When we compared the results to the experts segmentations we found that in 95% of the cases the maximum difference reached

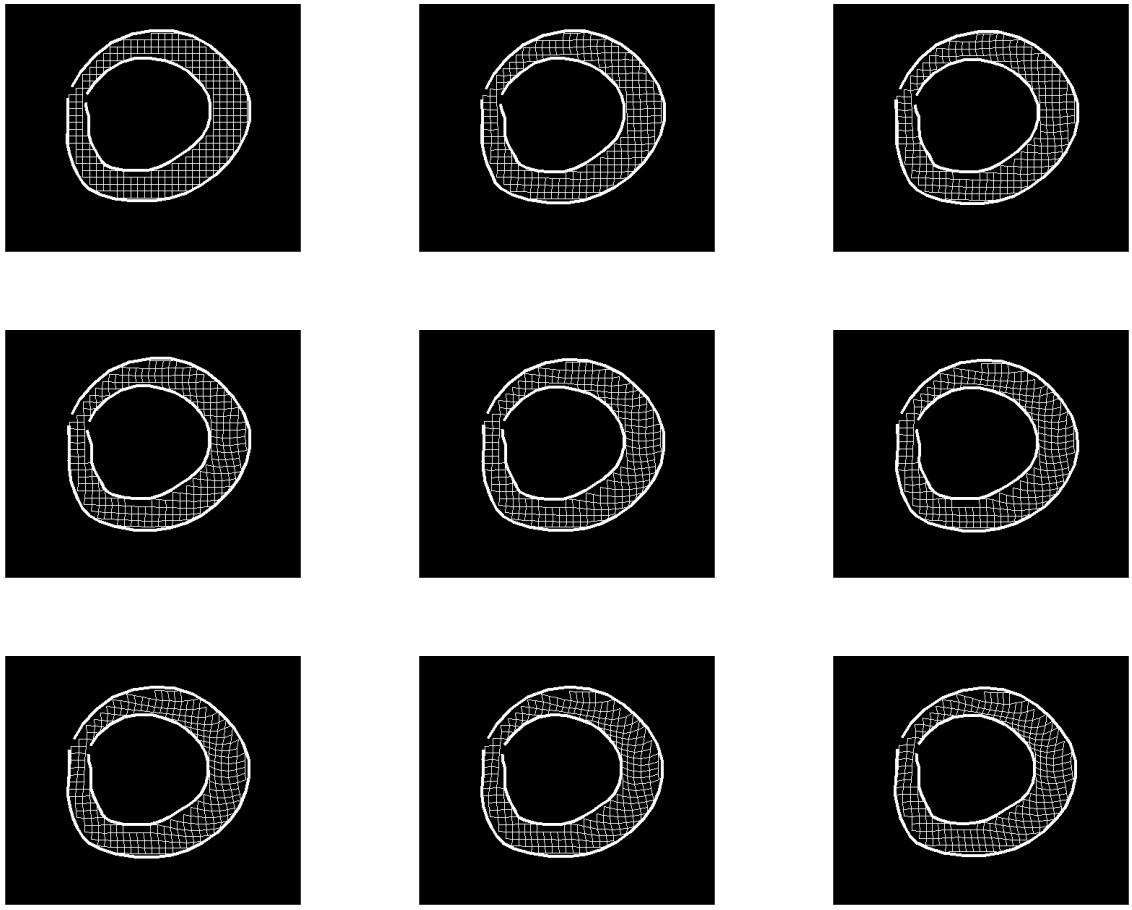

Figure 28: A synthetic grid overprinted over the myocardium and deformed by displacement map provided by HARP method in a middle SPAMM tagged sequence.

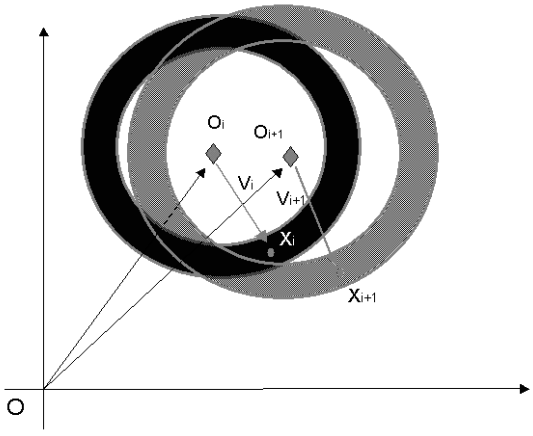

Figure 29: Scheme of the method used to calculate point rotation.

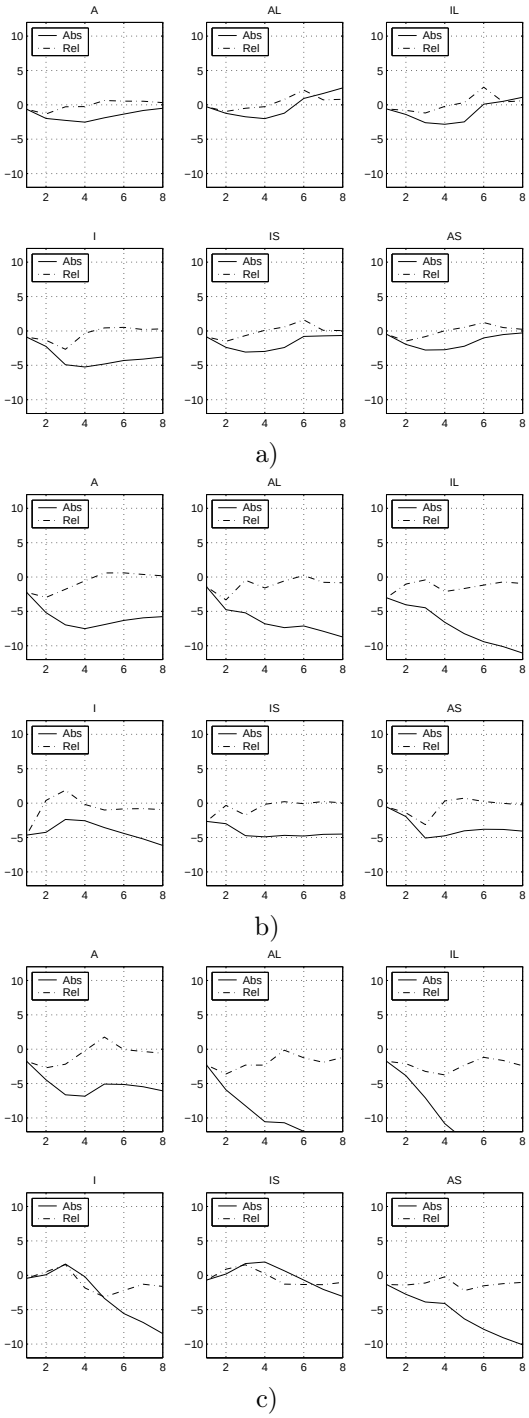

Figure 30: Rotation parameters for a healthy adult in each of the six myocardial zones in, basal a), mid b) and apical c) plane. Continuous curve represents total rotation (respect to the first frame), and dashed curve, the relative rotation to the previous frame.

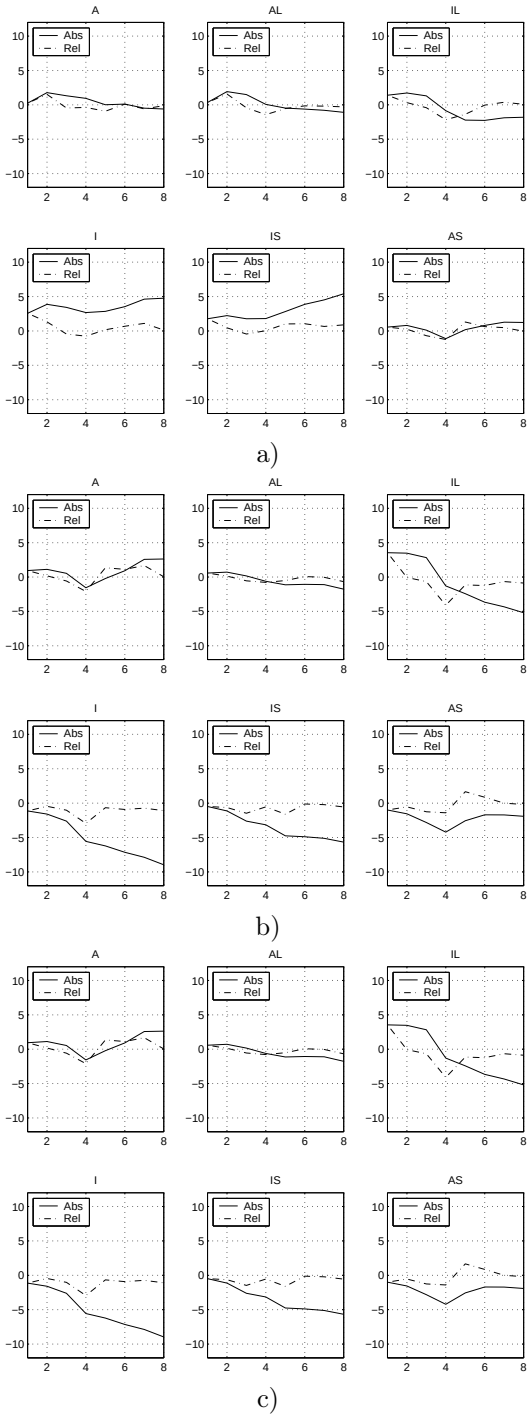

Figure 31: Rotation parameters for a pathological patient in each of the six myocardial zones in, basal a), mid b) and appical c) plane. Continuous curve represents total rotation (respect to the first frame), and dashed curve, the relative rotation to the previous frame.

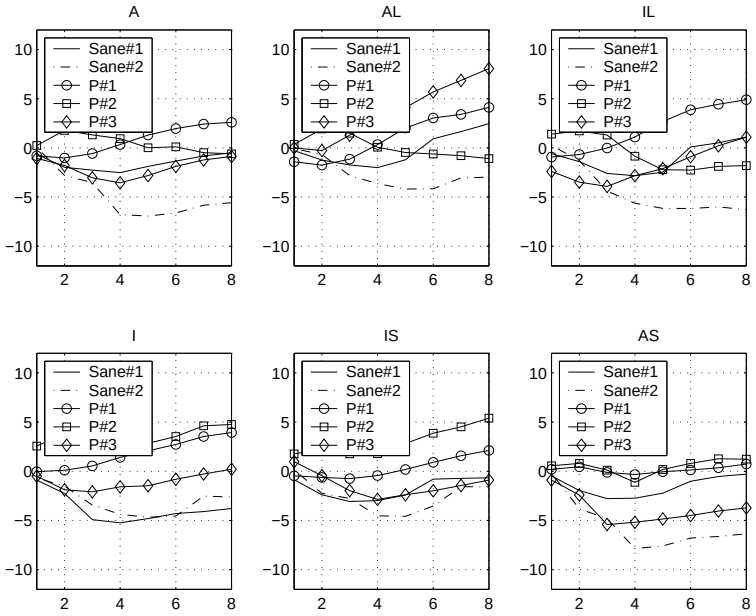

Figure 32: Rotation data mixed for healthy adults and patients with cardiac disease. Each plot belongs to a different myocardial zone and they belong to a middle plane.

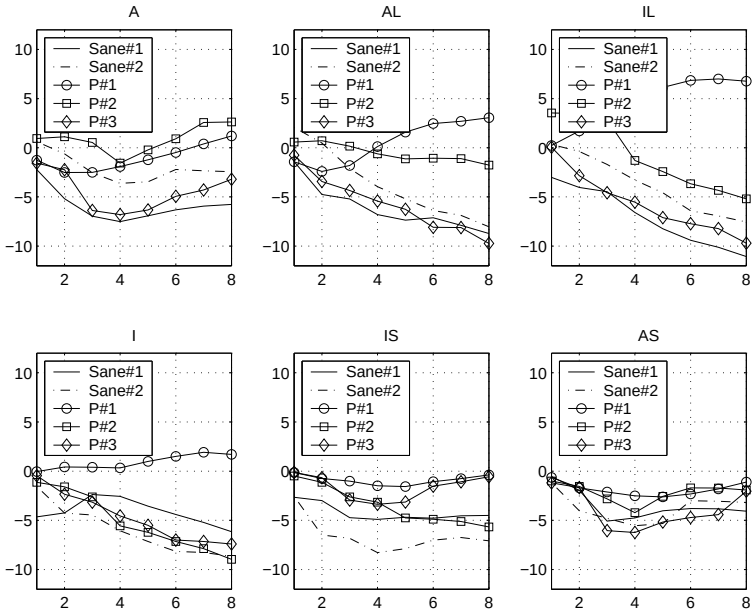

Figure 33: Rotation data mixed for healthy adults and patients with cardiac disease. Each plot belongs to a different myocardial zone and they belong to an apical plane.

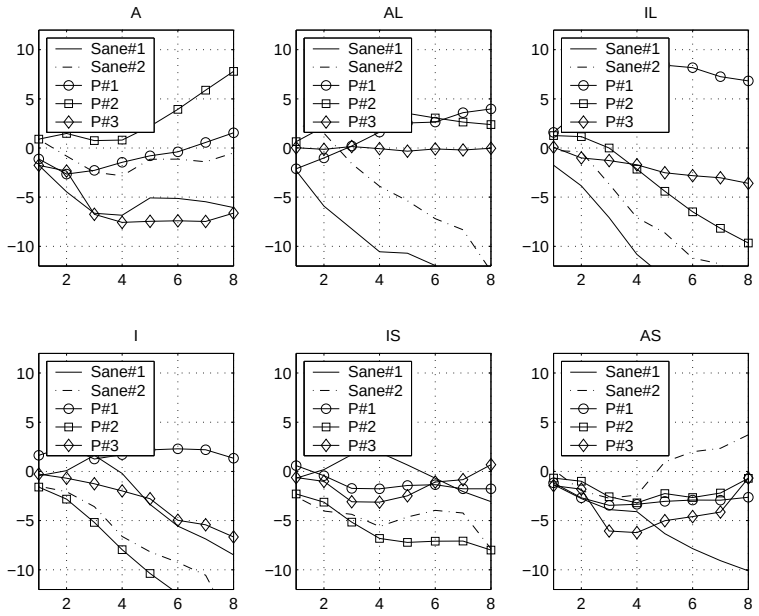

Figure 34: Rotation data mixed for healthy adults and patients with cardiac disease. Each plot belongs to a different myocardial zone and they belong to a basal plane.

was less than 12 pixels and the mean difference less than 4 pixels (Figure 35). Errors in segmentation are caused basically by a wrong initialization of the snake. In some frames, myocardium corners are not well defined (because of the image noise) and Harris corner detector can not deal with this. Another reason could be that the shape we are trying to segment do not belong to the learned shapes.

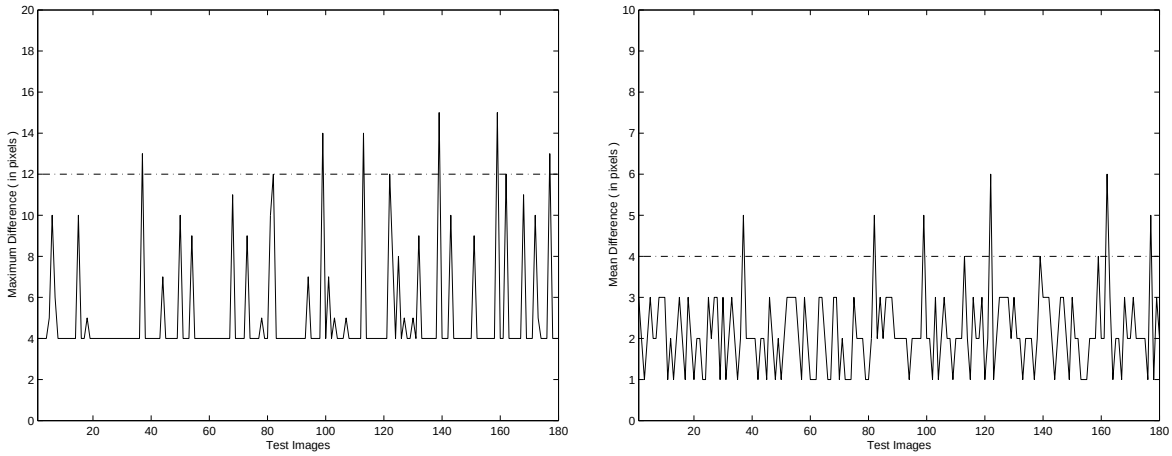

Figure 35: Maximum difference a) and mean difference b).

Finally notice that we have tested the algorithm independently from each frame without tacking advantage of the segmentation result obtained for the previous one. In practice, this is taken into account, thus Harris corner detector (which is prone to fail in presence of some drawbacks) have to be implemented just in the first frame where usually image artifacts are still not present. This leads to a more robust segmentation and probably improves results obtained in previous section.

9.2 On SPAMM Tagged MRI

Magnetic resonance images were obtained with a Phillips Intera Gyroscan 1,5 T magnetic resonance scanner (Phillips Medical Systems, Best, The Netherlands).

The results of the whole method will be tested in two ways. First of all we will test the HARP method performance which, as we have told, is the core for the prediction step; and second, we will test GASM framework in segmentation performance. In addition HARP method will be tested in both synthetic and real image sequences. Segmentation test in synthetic sequences makes no sense due to the fact that we see tag evolution restricted to myocardium structure and segmentation has already been done.

9.2.1 Synthetic Data

We have created a synthetic model based on the work presented in [72], where they have developed a full 3D model of a tagged LV. Nevertheless we adopt some of their ideas just to develop a 2D model that will allow us to create tagged MR sequences and which is governed by six parameters namely, translation in x and y, rotation, shear, eliptication and radial compression (Figure 36). These, properly mixed will lead to planar tagged LV sequences. From the synthetic sequence we know exactly its displacement map, which will be compared to the one given by the HARP algorithm.

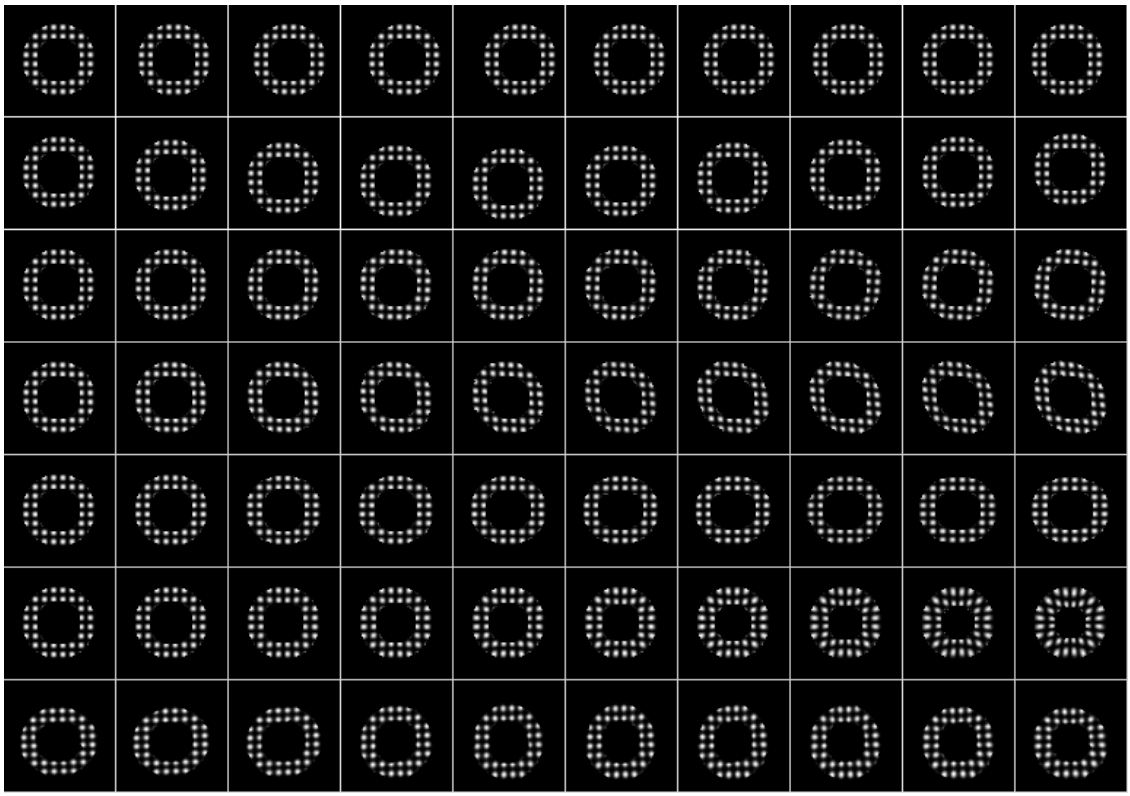

Figure 36: We can appreciate in the six first rows synthetic sequences varying for each one of the parameters x translation, y translation, rotation, shear, eliptication and radial compression. Last row mixes all the parameters to obtain a realistic movement of the tags.

Five synthetic sequences have been created and for each of them we have calculated the difference between both displacement maps at every point. Mean difference has been extracted. Results are shown

in Figure 37 where we can appreciate that error is almost the same (0.4 pixels) for every frame in the sequence. Tag evolution does not affect HARP performance in synthetic images. Nevertheless we will see that this is not true in real data.

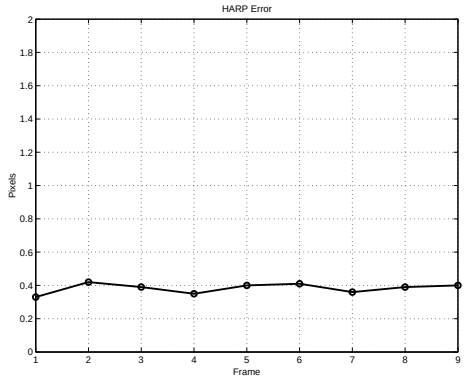

Figure 37: Mean of the distance error obtained in synthetic sequences

9.2.2 Real Data

HARP method testing on real data, has been done using 6 different patients whose tomographic scan volumes consisted of four SPAMM tagged sequences of the myocardium, each of them belonging to a different short axis plane: one to the appex, two to the middle and the last to the base. In each sequence we have manually tracked a set of eight points randomly distributed over the myocardium and compared the result with the displacement map provided by the HARP method. In Figure 38 .a, .b and .c we show the mean error of the method for the base, middle and appex planes respectively, and in Figure 38, the total mean error.

We can appreciate that error has grown in respect to the one obtained in synthetic sequences. The reason by which the same method applied to real images differs from previous results can be explained by the following:

- There is an image artifact in SPAMM tagged images that is worth to be mentioned. This is the longitudinal relaxation of magnetization, in virtue of which contrast between tags and tissue decreases (fading) (Figure 39 (a)). This affects directly to the harmonic peaks of the Fourier transform which are the base for HARP method making the method lose precision (Figure 39 (b)). This artifact occurs in latest frames of the sequence. In Figure 38 we can appreciate how fading artifact affects the HARP performance. From the sixth frame, error increases up to one pixel or more.

  There are some works that try to improve this lose of contrast as in [60]. Nevertheless the best way to improve this drawback is by applying CSPAMM tagging [73] (Complementary SPAtial Modulation of Magnetization) to images. This is an innovative technique of tagging to improve the contrast of tags and minimize their fading in latest frames of the sequence.

- Another characteristic from real images is that the acquisition plane in MR scan device is fixed while the heart moves a little along the long axis. This may cause to appear or disappear some tags (from other planes). Obviously this artifact does not appear in synthetic images. In the base planes, this artifact is accentuated because over-basal structures may appear. This explains why error in base is slightly greater than in appex or middle planes.

- Finally to mention that as frequency filter, we have chosen one for the first frame big enough to capture their movement for posterior frames while avoiding to overlap with neighboring peaks.

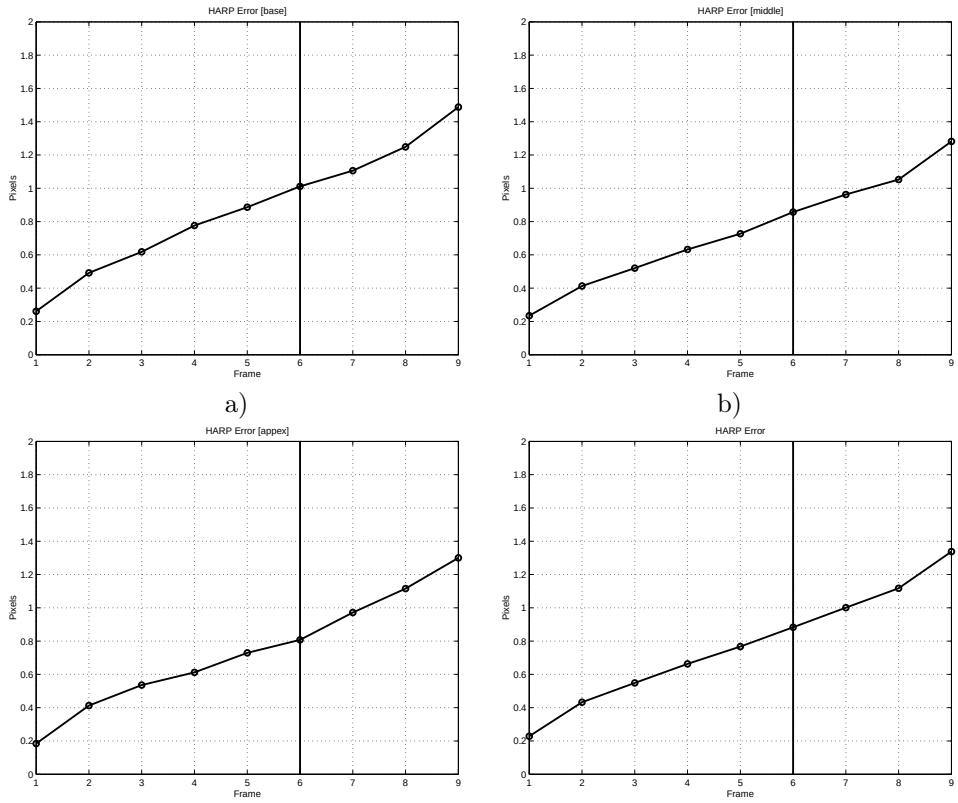

Figure 38: Mean error of HARP method performed on each frame at base a), middle b) and appex c). In the we appreciate total mean error.

Probably in real sequences the tag movement is greater than the one that initial filter can hold. In [74] they construct optimal band pass filters to obtain HARP images.

In regard to GASM segmentation performance, we mention that given an initial segmentation, the next one should have an error no greater than error appreciated in HARP tracking as this method is the core of the prediction step in GASM framework. Nevertheless applying just this first step (prediction) errors accumulate and segmentation performance fails. It is the second step (regularization) that overcomes this problem by applying a global correction over the proposed shapes and errors remain over the order of those appreciated in HARP performance.

A reason by which segmentation may fail, apart from previously mentioned drawbacks of the HARP method is that current myocardium shape does not belong to the PDM created from the training set. For this reason is important to assemble a shape set as complete as possible.

10 Conclusions

In medical imaging, automatic analysis of data provided by imaging scans is crucial in order to extract useful, reliable and reproducible quantitative data that physicians can interpret. In the analysis process, segmentation is the most important task to be performed and also the most difficult due to the fact that anatomical structures are not always well defined. For this reason, we encourage to use segmentation methods that incorporate as much a priori information about shape as possible. Thus, a method that fully

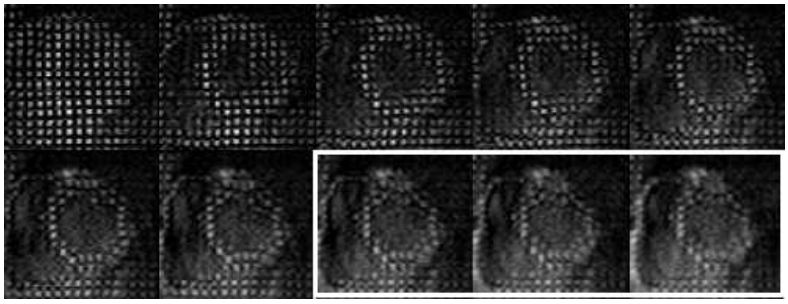

a)

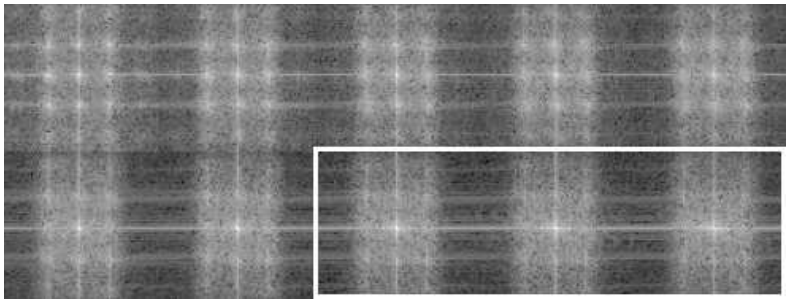

b)

Figure 39: We can appreciate the fading artifact that affects the last frames in SAPMM tagged sequences and also their Fourier transform. HARP method is damaged by this artifact causing a loss of precision of the method.

integrates the power of locally searching for possible contours such deformable models, with information about target structure, will lead to a robust method capable of dealing with most of medical imaging segmentation problems. GASM tries to fulfill this philosophy. It provides a general framework for image segmentation by mixing local searching in the prediction step with global shape correction given by the PDM in the regularization step. Despite the generality of GASM formulation, it is not a unique segmentation technique that can be applied to any problem, but it has to be tailored by designing an appropriate prediction step tacking into account both, image features and drawbacks. As instance, our prediction step in Contrast Echocardiography allowed the epicardial contours not to shrink the endocardial contours when not full structural information is available. By the other hand,using HARP method in SPAMM tagged MRI as prediction step, allowed us to derive a method able to track and segment at once and, in addition, to avoid useless calculations. In both problems, regularization step outperformed the result given by prediction step. Thus, different prediction steps implies different behavior and properties of the method.

GASM clearly improves any segmentation method performance by incorporating shape information as long as the training set is complete enough in the sense that it assembles all the variability that the structure might present.

11 Future Work

Our future work will be focused on two ways. The first one will be related to GASM where we will try to incorporate more a priori knowledge in order to provide of more robustness the method.

The second way relates to the special application of Tagged MRI: A first task to be done is to revise our HARP method in order to decrease the reported error in point tracking. To decrease segmentation error, we also will create a more complete PDM that can deal with as many as myocardium deformations as

possible and overcome the present drawback that some shapes are not contempled by the current model. And also we will apply ICA filters in order to improve tag detection.

It also will be of interest to derive other applications, apart from rotation, that allow to extract quantitative data prone to be used by the physicians, such as stress and strain. In order to facilitate their job, it would be of interest to create some user friendly interface that they can easily use to open new investigation lines.

A certain challenge will be to use orthogonal tagged planes (long axis) that allow us to derive 3D motion and extract any data in the whole heart volume.

An interesting issue will be to use our application in CSPAMM tagged images which will provide stability in tag contrast along the sequences and it will probably improve results.

References

[1] Terzopoulos, D. and Fleischer, K. (1988). Deformable models. The Visual Computer 4(6):306-331.

[2] Terzopoulos, D. (1986a). On matching deformable models to images. Technical Report 60, Schlumberger Palo Alto Research. Reprinted in Topical Meeting on Machine Vision, Technical Digest Series, Vol. 12 (Optical Society of America, Washington, DC) 1987, 160-167.

[3] Terzopoulos, D. (1986b). Regularization of inverse visual problems involving discontinuities. IEEE Trans. on Pattern Analysis and Machine Intelligence 8(4):413-424.

[4] Kass, M., Witkin, A. and Terzopoulos, D. (1988). Snakes: Active contour models. International Journal of Computer Vision 1(4):321-331.

[5] Radeva P, Serrat J. Rubber Snake: Implementation on Signed Distance Potential, Proc. of International Conference SWISS VISION'93, Zurich, Switzerland, September, pp.187-194, 1993.

[6] Berger, M.O. (1990). Snake growing. In Faugeras, O., ed., Computer Vision - Proc. First European Conf. on Computer Vision (ECCV'90), Antibes, France, April, 1990, Lectures Notes in Computer Science, 570-572. Springer-Verlag.

[7] Cohen, L.D. (1991). On active contour models and balloons. CVGIP: Image Understanding 53(2):211-218.

[8] Ueda, N. and Mase, K. (1992). Tracking moving contours using energy-minimizing elastic contour models. In Sandini, G., ed., Computer Vision - Proc. Second European Conf. on Computer Vision (ECCV'92), Santa Margherita Ligure, Italy, May, 1992, Lectures Notes in Computer Science, 453-457. Springer-Verlag.

[9] Rougon, N. and Preteux, F. (1993). Directional adaptive deformable models for segmentation with application to 2D and 3D medical images. In Medical Imaging 93: Image Processing, volume 1898 of SPIE Proc., 193-207. Bellingham, WA:SPIE.

[10] Cohen, L.D. and Cohen, I. (1993). Finite element methods for active contour models and balloons for 2D and 3D images. IEEE Trans. on Pattern Analysis and Machine Intelligence 15(11):1131-1147.

[11] Cohen, I., Ayache, N. and Sulger,P. (1992a). Tracking points on deformable objects using curvature information. In Sandini, G., ed., Computer Vision - Proc. Second European Conf. on Computer Vision (ECCV'92), Santa Margherita Ligure, Italy, May, 1992, Lectures Notes in Computer Science, 458-466. Springer-Verlag.

[12] Gupta, A., O'Donnell, T. and Singh, A. (1994). Segmentation and tracking of cine cardiac MR and CT images using a 3-D deformable model. In Proc. IEEE Conf. on Computers in Cardiology, September, 1994.

[13] Lin, W.C. and Chen, S.Y. (1989). A new surface interpolation technique for reconstructing 3D objects from serial cross-sections. Computer Vision, Graphics, and Image Processing 48:124-143.

[14] Chang, L.W., Chen, H.W. and Ho, J.R. (1991). Reconstruction of 3D medical images: A nonlinear interpolation technique for reconstruction of 3D medical images. Computer Vision, Graphics, and Image Processing 53(4):382-391.

[15] Amini, A.A., Weymouth, T.E. and Jain, R.C. (1990). Using dynamic programming for solving variational problems in vision. IEEE Trans. on Pattern Analysis and Machine Intelligence 12(9):855-867.

[16] Poon, C. S., Braun, M., Fahrig, R., Ginige, A. and Dorrell, A. (1994). Segmentation of medical images using an active contour model incorporating region-based images features. In Robb (1994), 90-97.

[17] Grzeszczuk, R.P. and Levin, D.N. (1994). Brownian strings: Segmenting images with stochastically deformable contours. In Robb (1994), 72-89.

[18] Rougon, N. and Preteux, F. (1991). Deformable markers: Mathematical morphology for active contour models control. In Image Algebra and Morphological Image Processing II, volume 1568 of SPIE Proc., 78-89. Bellingham, WA:SPIE.

[19] Chakraborty, A., Staib, L.H. and Duncan, J.S. (1994). Deformable boundary finding influenced by region homogeneity. In Proc. Conf. Computer Vision and Pattern Recognition (CVPR'94), Seattle, WA, June, 1994, 624-627. Los Alamitos, CA: IEEE Computer Society Press.

[20] Chakraborty, A. and Duncan, J.S. (1995). Integration of boundary finding and region-based segmentation using game theory. In Bizais et al. (1995), 189-200.

[21] Herlin, I.L., Nguyen, C. and Graffigne, C. (1992). A deformable region model using stochastic processes applied to echocardiographic images. In Proc. Conf. Computer Vision and Pattern Recognition (CVPR'92), Urbana, IL, June, 1992, 534-539. Los Alamitos, CA: IEEE Computer Society Press.

[22] Gauch, J.M., Pien, H.H. and Shah, J. (1994). Hybrid boundary-based and region-based deformable models for biomedical image segmentation. In Mathematical Methods in Medical Imaging III, volume 2299 of SPIE Proc., 72-83. San Diego, CA: SPIE.

[23] Leitner, F. and Cinquin, P. (1991). Complex topology 3D objects segmentation. In Model-Based Vision Development and Tools, volume 1609 of SPIE Proc., 16-26. Bellingham, WA: SPIE.

[24] Caselles, V., Catte, F., Coll, T. and Dibos, F. (1993). A geometric model for active contours. Numerische Mathematik 66.

[25] Malladi, R., Sethian, J. and Vemuri, B.C. (1995). Shape modeling with front propagation: A level set approach. IEEE Trans. on Pattern Analysis and Machine Intelligence 17(2):158-175.

[26] Caselles, V., Kimmel, R. and Sapiro, G. (1995). Geodesic active contours. In Proc. Fifth International Conf. on Computer Vision (ICCV'95), Cambridge, MA, June, 1995, 694-699. Los Alamitos, CA: IEEE Computer Society Press.

[27] Sapiro, G., Kimmel, R. and Caselles, V. (1995). Object detection and measurements in medical images via geodesic deformable contours. In Vision Geometry IV, volume 2573 of SPIE Proc., 366-378. Bellingham, WA: SPIE.

[28] Metaxas, D. and Terzopoulos, D. (1993). Shape and nonrigid motion estimation through physics-based synthesis. IEEE Trans. on Pattern Analysis and Machine Intelligence 15(6):580-591.

[29] Bardinet, E., Cohen, L.D. and Ayache, N. Superquadrics and free-form deformations: A global model to fit and track 3D medical data. In Ayache. 319-326.

[30] Bardinet, E., Cohen, L.D. and Ayache, N. Analyzing the deformation of the left ventricle of the heart with a parametric deformable model. Research report 2797, INRIA, Sophia-Antipolis, France.

[31] Bardinet, E., Cohen, L.D. and Ayache, N. A parametric deformable model to fit unstructured 3D data. Computer Vision and Image Understanding. In press. Also research report 2617, INRIA, Sophia-Antipolis, France.

[32] Hill, A., Thornham, A. and Taylor, C.J. (1993). Model-based interpretation of 3D medical images. In Proc. 4th British Machine Vision Conf. (BMVC'93), Surrey, UK, September, 1993, 339-348. BMVA Press.

[33] Cootes, T., Hill, A., Taylor, C. and Haslam, J. (1994). The use of active shape models for locating structures in medical images. Image and Vision Computing 12(6):355-366.

[34] Cootes T, Taylor C, Cooper D, Graham J. Active Shape Models - Their Training and application. Computer Vision and Image Understanding 1995; 61(1):38-59.

[35] Cootes T, Taylor C, Graham J. Training Models of Shape from Sets of Examples.

[36] Sharmeen Masood, 'Macroscopic Structure and Physiology of the Normal and Disease Heart', PhD thesis, supervised by G-Z Yang.

[37] Torrent-Guasp F., "La estructuración macroscópica del miocardio ventricular," Rev Esp Cardiol.,1980;33:265-287.

[38] Torrent-Guasp F., "Estructura y función del corazón," Rev Esp Cardiol.,1998;51:91-102.

[39] Torrent-Guasp F, Ballester M, Buckberg GD, Carreras F, Flotats A, Carrió I, Ferreira A, Samuels LE and Narula J., "Spatial Orientation of the Ventricular Muscle Band: physiologic contribution and surgical implications," J Thorac Cardiovasc Surg 2001; 122:389-92.

[40] Torrent-Guasp F, Ballester M, Caralps-Riera JM, Samuels LE and Narula J., "Spatial orientation of the ventricular muscle band and approach to partial ventriculotomy in heart failure,". In: "Heart Failure. Pathogenesis and treatment". Eds. Narula J, Virmani R, Ballester M, Carrió I, Westaby S, Frazier OH and Willerson JT. Martin Dunitz Ltd. 2002.

[41] Sano T, Takayama N and Shimamoto T., "Directional difference of conduction velocity in the cardiac ventricular syncytium studied by microelectrodes," Circ. Res. 1959;7:262-267

[42] Vladimir G. Fast, Bruce J. Darrow, Jeffrey E. Saffitz and Andre G. Kleber, "Anisotropic Activation Spread in Heart Cell Monolayers Assessed by High-Resolution Optical Mapping. Role of Tissue Discontinuities", Circ. Res., 1996;79:115-127

[43] J.C. Gower, Generalized Procrustes Analysis. Psychometrica. 40, 1975, 33-51.

[44] Herald B, Burns P N. Handbook of Contrast Echocardiography - Left ventricular function and myocardial perfusion.

[45] Malpica n, Santos A, Perez E, Garcia FernandezMA, Desco M. Reposicionamiento de Regiones de Interes en Secuencias de Ecocardiografia de Contraste.

[46] Desco M, et al. Myocardial Perfussion ssessment with Contrast Echocardiography. Ultrassonic Imaging 2001: Ultrassonic Imaging and Signal Processing. Proceedings of SPIE Vol. 4325 (2001). Imaging and Signal.

[47] Hamerneh G, Gustavsson T. Combining Snakes and Active Shape Models for Segmenting the Human Left Ventricle in Echocardiographic Images. IEEE Computers in Cardiology 2000 Vol.27.

[48] Dong, K.; Tabrizi, M.H.N.; Movahed, A.; Information Technology: Coding and Computing, 2000. Proceedings. International Conference on , 27-29 March 2000 Pages: 477 - 482.

[49] Brigger, P.; Bacharach, S.; Aldroubi, A.; Unser, M.; Image Processing, 1997. Proceedings., International Conference on, Volume: 2 , 26-29 Oct. 1997 Pages: 113 - 116 vol.2.

[50] Yang, G.Z.; Gatehouse, P.D.; Panting, J.; Burger, P.; Pennell, D.J.; Firmin, D.N.; Image Processing and Its Applications, 1997., Sixth International Conference on , Volume: 2 , 14-17 July 1997 Pages: 838 - 842 vol.2

[51] Spreeuwers L.J., F. Wierda F., Breeuwer M.; Optimal Myocardial Boundary Estimation for MR Cardio Perfusion Measurements Using Sensitivity Analysis.

[52] Weickert J. Anisotropic Diffusion in Image Processing.

[53] Garcia J., Rotger D.,Carreras F., Leta R., Radeva P. (2003). Contrast Echography Segmentation and Tracking by Trained Deformable Models. In Proc. IEEE Conf. on Computers in Cardiology, Volume: 30 173 - 176 September, 2003.

[54] Masood S, Yang GZ, Pennell DJ, Firmin DN, 'Investigating intrinsic myocardial mechanics: the role of MR tagging, velocity phase mapping, and diffusion imaging', Journal of Magnetic Resonance Imaging, 12(6):873-83, 2000 Dec.

[55] L. Axel and L. Dougherty, 'MR imaging of motion with spatial modulation of magnetization', Radiology, 171:841-845, 1989.

[56] L. Axel and L. Dougherty, 'Heart wall motion: improved method of spatial modulation of magnetization for MR imaging', Radiology, 172:349, 1989.

[57] Leon Axel, Roberto C. Goncalves and Daniel Bloomgarden, 'Regional Heart Wall Motion: Two-dimensional Analysis and Fuctional Imaging with MR Imaging', Radiology, 183(3):745-50, 1992 June.

[58] A.A. Young and L. Axel, "Three-dimensional motion and deformation of the heart wall: Estimation with spatial modulation of magnetization- A model-based approach," Radiology 1992;185:241-247.

[59] S. Zhang, M. A. Douglas, L. Yaroslavsky, R. M. Summers, V. Dilsizian, L. Fananapazir and S.L. Bacharach, "A Fourier based algorithm for tracking SPAMM tags in gated magnetic resonance cardiac images," Med Phys., 1996;23:1359-1369.

[60] M.A.M. Groot Koerkamp, G.Snoep, A.M.M. Muijtjens and G.J. Kemerink, "Improving Contrast and Tracking of Tags in Cardiac Magnetic Resonance Images," Magn. Res. in Med.,1999;41:973-982.

[61] P. Radeva, A. A. Amini and J.Huang, "Deformable B-solids and implicit snakes for 3D localization and tracking of SPAMM MRI Data," Comput. Vis. Image Underst. 1997;66:163-178.

[62] Guttman, M.A.; Prince, J.L.; McVeigh, E.R.; Tag and contour detection in tagged MR images of the left ventricle Medical Imaging, IEEE Transactions on ,Volume: 13 , Issue: 1 , March 1994 Pages:74 - 88.

[63] C. Ozturk and E. McVeigh, "Four dimensional B-spline based motion analysis of tagged cardiac MR images, SPIE Medical Imaging, San Diego, CA, February 1999.

[64] Osman, N.F.; Prince, J.L.; Angle images for measuring heart motion from tagged MRI; Image Processing, 1998. ICIP 98. Proceedings. 1998 International Conference on ,Volume: 1 , 4-7 Oct. 1998 Pages:704 - 708 vol.1.

[65] Osman N.F, Prince J.L.; Visualizing myocardial function using HARP MRI; Phys. Med. Biol. vol. 45 (2000) Pages:1665 - 1682.

[66] Osman, N.F.; McVeigh, E.R.; Prince, J.L.; Imaging heart motion using harmonic phase MRI; Medical Imaging, IEEE Transactions on ,Volume: 19 , Issue: 3 , March 2000 Pages:186 - 202.

[67] L. Pan, J.A.C. Lima and N.F. Osman, "Fast tracking of cardiac motion using 3D-HARP".

[68] I. Haber and C.F. Westin, "Model-based 3D Tracking of Cardiac Motion in HARP Images," Proc. Intl. Soc. Mag. Res. Med., 2002;10.

[69] W.G. O'Dell, C.C. Moore, W.C. Hunter, E.A. Zerhouni, and E.R. McVeigh, "Three-dimensional myocardial deformations: Calculations with displacement field fitting of tagged MR images", Radiology, vol. 195, pp. 829-835, 1995.

[70] T.S. Denney and J.L. Prince, "Reconstruction of 3-D left ventricular motion from planar tagged cardiac MR images: An estimation theoretic approach", IEEE Trans. Med. Imag., vol. 14, pp. 625-635, 1995.

[71] N.F. Osman, W.S. Kerwin, E.R. McVeigh, and J.L Prince, "Cardiac motion tracking using CINE harmonic phase (HARP) magnetic resonance imaging", Megnetic Resonance in Medicine 42, pp. 1048-1060, 1999.

[72] E. Waks, J.L. Prince, and A. Douglas, "Cardiac Motion Simulator for Tagged MRI", Proceedings of the IEEE Workshop on Mathematical Methods in Biomedical Image Analysis, San Francisco June 21-22, 1996.

[73] Fischer SE, McKinnon GC, Maier SE, Boesiger P., 'Improved myocardial tagging contrast', Journal of Magnetic Resonance and Medicine, 30(2):191-200, August 1993.

[74] Osman, N.F.; Prince, J.L.; 'Onthe design of the bandpass filters in Harmonic Phase MRI',Image Processing, 2000. Proceedings. 2000 International Conference on , Volume: 1 , 10-13 Sept. 2000 Pages:625 - 628 vol.1.

[75] Jonathan Myers, PhD, Doris Wagner, MD, Thomas Schertler, MD, Meinrad Beer, MD, Roger Luchinger, MD, Maya Klein, MD, Hans Rickli, MD, Peter Muller, MD, Kurt Mayer, MD,Juerg Schwitter, MD, and Paul Dubach; 'Effects of exercise training on left ventricular volumes and function in patients with nonischemic cardiomyopathy: Application of magnetic resonance myocardial tagging'; Zurich, Switzerland, and Palo Alto, Calif.

[76] Helen C. Oxenham, Alistair A. Young, Brett R. Cowan, Thomas L. Gentles, Christopher J. Occleshaw, Carissa G. Fonseca, Robert N. Doughty, and Norman Sharpe; 'Age-Related Changes in Myocardial Relaxation Using Three-Dimensional Tagged Magnetic Resonance Imaging'; JOURNAL OF CARDIOVASCULAR MAGNETIC RESONANCEVol. 5, No. 3, pp. 421-430, 2003.

[77] R. E. HENSON, S. K. SONG, J. S. PASTOREK, J. J. H. ACKERMAN, AND C. H. LORENZ; 'Left ventricular torsion is equal in mice and humans'; Am J Physiol Heart Circ Physiol 278: H1117-H1123, 2000.

[78] Ledesma M.J., Malpica N., Santos A., García-Fernéndez M.A., Desco M., "Quantification Methods in Contrast Echocardiography". En: Contrast echocardiography in clinical practice. Ed: M.A. García Fernández. Springer Verlag, 69-89, 2004.

[79] Ewi K., Jayaweera A.R., Firoozan S., Linka A., Skyba D.M., Kaul S., "Quantification of Myocardial Blood Flow with Ultrassound-induced Destruction of Microbubbles Administred as a Constant Venous Infusion" Circulation, vol. 97 no.5, pp. 473-483, 1998.

[80] Barron J.L., Fleet D.J., Beauchemin S.S., "Performance of Optical Flow Techniques", International Journal of Computer Vision, vol. 12, no. 1, pp. 43-77, 1994.

[81] Ledesma-Carbayo M.J., Kybic J., Desco M., Santos A., Unser M., "Cardiac Motion Analysis from Ultrasound sequences Using Non-Rigid Registration", Medical Image Computing and Computer-Assisted Intervention (MICCAI), Utrecht, Lecture Notes in Computer Science, Springer, 2001.